Icarus 245 (2015) 38–55

Contents lists available at ScienceDirect

Icarus

journal homepage: www.elsevier.com/locate/icarus

A radar survey of M- and X-class asteroids. III. Insights into their composition, hydration state, & structure

Michael K. Shepard [a,*], Patrick A. Taylor [b], Michael C. Nolan [b], Ellen S. Howell [b], Alessondra Springmann [b], Jon D. Giorgini [c], Brian D. Warner [d], Alan W. Harris [e], Robert Stephens [f], William J. Merline [g], Andrew Rivkin [h], Lance A.M. Benner [c], Dan Coley [i], Beth Ellen Clark [j], Maureen Ockert-Bell [j], Christopher Magri [k]

[a] Bloomsburg University, 400 E. Second St., Bloomsburg, PA 17815, USA
[b] NAIC/Arecibo Observatory, HC 3 Box 53995, Arecibo, PR 00612, USA
[c] Jet Propulsion Laboratory, California Institute of Technology, Pasadena, CA 91109, USA
[d] More Data! Inc., Eaton, CO 80615, USA
[e] More Data! Inc., La Cañada, CA 91011, USA
[f] More Data! Inc., Rancho Cucamonga, CA 91730, USA
[g] Southwest Research Institute, Boulder, CO 80302, USA
[h] Johns Hopkins University Applied Physics Laboratory, Laurel, MD, 20723, USA
[i] Center for Solar System Studies, Rancho Cucamonga, CA 91730, USA
[j] Ithaca College, Ithaca, NY 14853, USA
[k] University of Maine at Farmington, Farmington, ME, 04938, USA

ARTICLE INFO

Article history:
Received 16 February 2014
Revised 5 September 2014
Accepted 10 September 2014
Available online 21 September 2014

Keywords:
Asteroids
Asteroids, composition
Asteroids, surfaces

ABSTRACT

Using the S-band radar at Arecibo Observatory, we observed thirteen X/M-class asteroids; nine were previously undetected and four were re-observed, bringing the total number of Tholen X/M-class asteroids observed with radar to 29. Of these 29M-class asteroids, 13 are also W-class, defined as M-class objects that also display a 3-μm absorption feature which is often interpreted as the signature of hydrated minerals (Jones, T.D., Lebofsky, L.A., Lewis, J.S., Marley, M.S. [1990]. Icarus 88, 172–192; Rivkin, A.S., Howell, E.S., Britt, D.T., Lebofsky, L.A., Nolan, M.C., Branston, D.D. [1995]. Icarus 117, 90–100; Rivkin, A.S., Howell, E.S., Lebofsky, L.A., Clark, B.E., Britt, D.T. [2000]. Icarus 145, 351–368).

Consistent with our previous work (Shepard, M.K. et al. [2008]. Icarus 195, 184–205; Shepard, M.K., Harris, A.W., Taylor, P.A., Clark, B.E., Ockert-Bell, M., Nolan, M.C., Howell, E.S., Magri, C., Giorgini, J.D., Benner, L.A.M. [2011]. Icarus 215, 547–551), we find that 38% of our sample (11 of 29) have radar albedos consistent with metal-dominated compositions. With the exception of 83 Beatrix and 572 Rebekka, the remaining objects have radar albedos significantly higher than the mean S- or C-class asteroid (Magri, C., Nolan, M.C., Ostro, S.J., Giorgini, J.D. [2007]. Icarus 186, 126–151).

Seven of the eleven high-radar-albedo asteroids, or 64%, also display a 3-μm absorption feature (W-class) which is thought to be inconsistent with the formation of a metal dominated asteroid. We suggest that the hydration absorption could be a secondary feature caused by low-velocity collisions with hydrated asteroids, such as CI or CM analogs, and subsequent implantation of the hydrated minerals into the upper regolith. There is recent evidence for this process on Vesta (Reddy, V. et al. [2012]. Icarus 221, 544–559; McCord, T.B. et al. [2012]. Nature 491, 83–86; Prettyman, T.H. et al. [2012]. Science 338, 242–246; Denevi, B.W. et al. [2012]. Science 338, 246–249).

Eleven members of our sample show bifurcated radar echoes at some rotation phases; eight of these are high radar albedo targets. One interpretation of a bifurcated echo is a contact binary, like 216 Kleopatra, and several of our sample are contact binary candidates. However, evidence for other targets indicates they are not contact binaries. Instead, we hypothesize that these asteroids may have large-scale variations in surface bulk density, i.e. isolated patches of metal-rich and silicate-rich regions at the near-surface, possibly the result of collisions between metal and silicate-rich asteroids.

* Corresponding author at: Dept. of Environmental, Geographical, and Geological Sciences, Bloomsburg University of Pennsylvania, 400 E. Second St., Bloomsburg, PA 17815, USA. Fax: +1 570 389 3028.

E-mail address: mshepard@bloomu.edu (M.K. Shepard).

http://dx.doi.org/10.1016/j.icarus.2014.09.016
0019-1035/

1. Introduction

The Tholen (1984) X-class asteroids are defined by featureless spectra with red slopes and an unknown visual albedo. The Bus X-complex is similar (Bus and Binzel, 2002). Asteroids with these spectral characteristics and visual albedos in the range ~0.10–0.30 are classified as Tholen M-class. Historically, M-class asteroids were thought to be the denuded metallic cores of disrupted parent bodies or possibly enstatite chondrites (Chapman and Salisbury, 1973; Gaffey, 1976; Gaffey and McCord, 1979; Bell et al., 1989; Cloutis et al., 1990).

Since 2004, we have undertaken a systematic survey of all the Tholen (1984) X/M-class asteroids within the detectability range of the Arecibo radar facility. Because the visible/near-infrared (VISIR) spectral data for this class are ambiguous, radar is a better tool for identifying metallic content in the upper meter or so of the regolith. Our previous work (Shepard et al., 2008, 2010, 2011; Ockert-Bell et al., 2008, 2010) found that only 30–40% of the M-class have radar albedos consistent with metal-dominated compositions and the disrupted core interpretation. The remainder have surface regolith bulk densities higher than is typical of other main belt asteroids (Shepard et al., 2010) and are likely to be metal rich, but not dominated by metal.

A number of spectral surveys of the X-/M-class have revealed that roughly half of the M-class exhibit subtle silicate absorption features near 0.9 and 1.9 μm, commonly attributed to pyroxenes (Clark et al., 2004; Hardersen et al., 2005, 2011; Birlan et al., 2007; Ockert-Bell et al., 2008, 2010; Fornasier et al., 2011).

One puzzling observation of numerous M-class asteroids is the evidence of a 3 μm absorption feature, often attributed to hydrated minerals (Jones et al., 1990; Rivkin et al., 1995, 2000). M-class asteroids with this characteristic are referred to as W-class by Rivkin et al. (2000) and are thought to be inconsistent with both the metallic core and enstatite chondrite interpretation (Hardersen et al., 2005, 2011). However, Shepard et al. (2008) found that one W-class asteroid, 129 Antigone, has the high radar reflectivity of a metal dominated object. Other suggested M-asteroid analogs that may have hydrated phases include the CH/CB meteorites and carbonaceous chondrites (CI and CM) (Cloutis et al., 1990; Vilas, 1994; Rivkin et al., 2000; Hardersen et al., 2005, 2011). However, the bulk density of the CI/CM analogs is low because of low metal content and they are therefore inconsistent with the higher than average radar albedos observed in the M-class (Shepard et al., 2010). Prior to the work reported here, Antigone was a singular anomaly. As we describe below, this is no longer the case and the coexistence of metal and hydrated phases must be reconciled.

In this paper, the third compilation of our work, we report on recent observations of thirteen M-class asteroids: nine previously undetected with radar and four re-observations. This work extends the total number of radar detected M-class main-belt asteroids to 29, 45% more than in our previous work.

The paper is outlined as follows. In Section 2, we briefly discuss the conventions, equations, and physical interpretations used in our radar analysis. In Section 3, we describe the results for our new radar data sets along with individual object analysis. In Section 4, we examine the results in mass and discuss their ramifications for understanding the X/M-class complex.

2. Conventions, equations, and physical interpretations

In this section we review the conventions and equations that describe the relationship between radar, thermal, and optical measurements and the physical properties of these asteroids used in this paper. These are essentially identical with those summarized in Shepard et al. (2010) but are repeated here for convenience.

2.1. Asteroid shape, size, rotation period, and optical properties

To place constraints on a target's diameter, we use the following relationship between effective diameter (D_{eff}, in km), visual albedo (p_v), and absolute magnitude (H) (Pravec and Harris, 2007):

$$\log D_{eff}\ (\mathrm{km}) = 3.1235 - 0.2H - 0.5 \log p_v \tag{1}$$

The effective diameter D_{eff} is the diameter of a sphere with the same projected area as the asteroid.

We assume each asteroid can be modeled as a triaxial ellipsoid with long, intermediate, and short axes of 'a', 'b', and 'c', respectively. The c-axis is assumed to be the rotation axis. We characterize the shape of the ellipsoid with the ratios of these axes: a/b and a/c or b/c.

We report published diameters where available; the majority are from thermal measurements obtained with IRAS (Tedesco et al., 2002), WISE (Masiero et al., 2011), and AKARI (Usui et al., 2011). Where possible, we adopt a mean of those measurements available and assume uncertainties of at least ±5% to take into account both the (smaller) random uncertainties quoted for each reported diameter and potentially larger systematic uncertainties (Lebofsky, 1989; Masiero et al., 2011; Usui et al., 2011).

Unless otherwise noted, all rotation periods and lightcurve amplitudes are taken from the asteroid lightcurve database and references therein (Warner et al., 2009a). Uncertainties in the rotation periods are on the order of the last significant digit.

2.2. Radar analysis

Each observing cycle or "run" consisted of transmission of a circularly polarized 2380 MHz (12.6 cm) signal for the round-trip light travel time to the target, followed by reception of echoes for a similar duration in the opposite (OC) and same (SC) senses of circular polarization as transmitted. We measured the radar cross-sections of our targets (in km^2) σ_{OC} and σ_{SC}, by integrating the continuous wave (CW) power spectra. These are equivalent to the cross-sectional areas of a smooth, metallic sphere (a perfect reflector) that would generate the observed echo power when viewed at the same distance.

For an asteroid observed at S-band (2380-MHz), its apparent width (in km), $D(\phi)$, normal to the apparent spin vector at rotation phase ϕ, is related to the instantaneous bandwidth B (in Hz) of the radar echo (due to the apparent rotation), the rotation period, and asteroid orientation by

$$D(\phi) = \frac{PB(\phi)}{27.7 \cos \delta} \tag{2}$$

where P is the apparent (synodic) rotation period in hours and δ is the sub-radar latitude. For each target we estimate the minimum bandwidth. In the absence of information about the pole orientation and sub-radar latitude δ, we assume an equatorial view ($\delta = 0$) to get a lower bound on the maximum pole-on breadth, D_{max}. Our experience with asteroids of weak to moderate signal-to-noise ratio (SNR) (optimally filtered sum SNR $\leqslant$ 20 or so) suggests that we can obtain a reasonable estimate of the bandwidth using the points where echo power drops to zero standard deviations (zero-crossing bandwidth or B_{ZC}) after smoothing in frequency to boost the SNR. For signals with higher SNR, we often adopt the points at which the echo drops below two standard deviations of noise ($B_{2\sigma}$). Uncertainties are typically based on the frequency resolution of the spectrum. In a few instances, we adopt a bandwidth, B, which is somewhat narrower based upon the waveform behavior, and adopt conservative uncertainties. We get a sense for the goodness of a bandwidth estimate by comparing it to the bandwidth of the optimal filter for maximizing the signal-to-noise ratio, referred to as the "effective frequency resolution", or "effective resolution." In

general, this is narrower than the estimated bandwidth, but it should be comparable.

The circular polarization ratio, μ_c, is defined to be the ratio of the SC and OC echo power:

$$\mu_c = \frac{\sigma_{SC}}{\sigma_{OC}} \tag{3}$$

Values larger than zero are thought to be caused by wavelength-scale near-surface (~1 m depth for 12.6 cm wavelength) roughness and inhomogeneities and/or subsurface or multiple scattering. Polarization ratios approaching 0.0 are thought to arise from smooth surfaces, while values near 0.3 are observed on moderately rough surfaces such as found on 25143 Itokawa and 433 Eros (Ostro et al., 2005; Magri et al., 2001). Because systematic uncertainties are nearly the same for both polarization senses, uncertainties in circular polarization ratio are dominated by receiver thermal noise. Unless otherwise stated, our quoted uncertainties for random errors are one standard deviation.

The OC radar albedo, $\hat{\sigma}_{OC}$, of an asteroid is defined to be the ratio of its OC radar cross section (σ_{OC}) to its cross-sectional area,

$$\hat{\sigma}_{OC} = \frac{4\sigma_{OC}}{\pi D_{eff}^2} \tag{4}$$

$\hat{\sigma}_{OC}$ can vary with rotation and aspect. Published MBA radar albedos vary from a low of 0.039 for the CP-class main-belt asteroid (MBA) 247 Eukrate (Magri et al., 2007) to a maximum of 0.6 for the M-class 216 Kleopatra (Ostro et al., 2000). Uncertainties in our estimates of absolute radar cross-section are usually ±25% and are based on estimates of systematic uncertainties in transmitted power and calibration.

For targets with higher SNRs, we may transmit a coded-waveform pulse and deconstruct the echo into a delay-Doppler image; essentially, we extract a second dimension – time delay – from the echo. These can be displayed as delay-Doppler images, traditionally with Doppler frequency along the *x*-axis and delay-time along the *y*-axis. The advantage of delay-Doppler imaging is that we can estimate the diameter of the target by assuming the visible delay-depth (range of delay-time from leading edge to visible echo end times half the speed of light) to be an estimate of its radius, assuming a more-or-less spherical target.

2.3. Radar albedo and surface bulk density

Shepard et al. (2010) developed a model to relate radar albedo to surface regolith bulk density. The model is a piece-wise function based on previous models by Ostro et al. (1985) and Garvin et al. (1985) and gives results consistent with our current understanding of the composition and porosity of main-belt asteroids. Given the OC radar albedo, $\hat{\sigma}_{OC}$, or surface bulk density, ρ (in g cm^{-3}) we can find the other via:

$$\begin{aligned} \hat{\sigma}_{OC} &= 1.2\tanh^2\left(\frac{\rho}{6.4}\right) \quad \text{for} \quad \rho \leqslant 1.57 \text{ g cm}^{-3} \\ \hat{\sigma}_{OC} &= 0.144\rho - 0.156 \quad \text{for} \quad \rho > 1.57 \text{ g cm}^{-3} \\ &\text{or} \\ \rho &= 3.20\ln\left(\frac{1+\sqrt{0.83\hat{\sigma}_{OC}}}{1-\sqrt{0.83\hat{\sigma}_{OC}}}\right) \quad \text{for} \quad \hat{\sigma}_{OC} \leqslant 0.07 \\ \rho &= 6.944\hat{\sigma}_{OC} + 1.083 \quad \text{for} \quad \hat{\sigma}_{OC} > 0.07 \end{aligned} \tag{5}$$

Using this model, Shepard et al. (2010) proposed the sub-classification of Mm for M-class asteroids displaying radar albedos of ~0.39 or higher at *some* rotation phases. In this paper, we modify this slightly and consider an asteroid with a *mean* radar albedo ⩾0.30 to be dominated by metal. This would be consistent with a mix of 70% Fe/Ni, 30% silicate with $\rho = 3.0$ g cm^{-3}, and 50% surface bulk porosity.

3. New radar observations of M-class MBAs

In this section, we summarize the radar observations of thirteen M-class MBAs; nine are newly observed and four were observed previously. We have organized this section by object, putting observations and analysis together, instead of separating those sections in a more traditional manner. Observing circumstances for all targets are given in Tables 1 and 2 list the measured radar properties of each target.

3.1. (77) Frigga

Frigga has reported diameters of $D_{eff} = 69 \pm 2$ km (IRAS), 67.2 ± 1 km (WISE), and 65.8 ± 0.16 km (AKARI) and associated optical albedos of $p_v = 0.14 \pm 0.01$, 0.15 ± 0.05, and 0.16 ± 0.01 respectively; we adopt $D_{eff} = 68 \pm 4$ km and $p_v = 0.15 \pm 0.01$. It has a rotational period of $P = 9.012$ h (Warner et al., 2009a). It is classified as MU (unusual M) in the Tholen system, and Xe in the Bus and Binzel (2002) system. Rivkin et al. (2000) observed a 3 μm absorption feature which they attributed to the presence of hydrated phases and classified Frigga as a W. No rotational pole or shape has been reported.

Visible and near-IR spectra of Frigga show reddening in the visible, rolling over in the near infrared. Hardersen et al. (2011) find Frigga's spectrum essentially featureless, others report evidence of a subtle absorption feature at 0.87 μm usually attributed to low-Fe, low-Ca orthopyroxenes (Ockert-Bell et al., 2008, 2010; Takir et al., 2008).

We observed Frigga at Arecibo on 17 December 2011 and from 26 to 28 January 2012 (Table 1), obtaining a total of 9 runs. For the weighted sum of all echoes, we obtained a SNR of 20 and measured a bandwidth $B_{ZC} = 152 \pm 20$ Hz, constraining $D_{max} > 50$ km. Assuming the adopted diameter of 68 km, we would expect an equatorial bandwidth of 209 Hz; using Eq. (2), our results therefore imply a sub-radar latitude (or observational aspect) of 43° ± 10°. We measured an OC cross-section $\sigma_{OC} = 530 \pm 130$ km^2 and polarization ratio $\mu_c = 0.03 \pm 0.05$. The former leads to an OC radar albedo of $\hat{\sigma}_{OC} = 0.14 \pm 0.04$ which is typical for a main-belt asteroid and suggests only a low to modest metal content in the upper meter or so of the regolith. The low polarization ratio is indicative of a smooth near-surface.

Fig. 1 shows the individual radar runs of Frigga and Fig. 2 shows the sum of all runs. Two runs, #3 and #4 at similar rotational longitudes, show evidence for a large concavity or bifurcation based on the shape of the echo (the twin peaks). However, the echoes of runs #5 and 6, rotated approximately 180° from #3 and #4 have much lower SNRs. Similar behavior has been observed in other M-class objects (Shepard et al., 2010).

3.2. (92) Undina

Undina has reported diameters of $D_{eff} = 126 \pm 4$ km (IRAS) and 121 ± 2 km (AKARI), and associated optical albedos of $p_v = 0.25 \pm 0.02$ and 0.28 ± 0.01, respectively. We adopt $D_{eff} = 123 \pm 6$ km and $p_v = 0.26 \pm 0.02$. Its rotation period $P = 15.941$ h (Warner et al., 2009a). It is classified as a Tholen X-class, but its optical albedo puts it into the M-class; it is classified as an Xc in the Bus and Binzel scheme.

Fornasier et al. (2011) measured a VISIR spectrum of Undina and report a red spectrum with absorption features at 0.51 μm, "similar to Fe^{2+} spin-forbidden crystal field transitions seen in

Table 1
Observing circumstances.

Target	Date	RA (°)	DEC (°)	λ (°)	β (°)	Dist AU	Total runs	OC SNR
77 Frigga	2011 December 17	100	27	99	4	1.57	1	7
	2012 January 26–28	120	24	117	3	1.48	8	20
92 Undina	2011 November 11–14	66	12	66	−9	2.13	4	25
110 Lydia	2012 October 15–18	40	11	41	−4	1.70	7	40
161 Athor	2013 November 13–14	48	27	53	9	1.41	3	10
201 Penelope	2011 November 11, 14	47	8	47	−9	1.46	2	16
261 Prymno	2011 November 19, 2011 December 14-16	79	21	80	−2	1.30	4	19
359 Georgia	2012 October 15, 17	7	5	8	2	1.37	3	10
413 Edburga	2011 November 12–14	80	1	79	−22	1.12	3	16
441 Bathilde	2011 December 17–18	91	20	91	−3	1.61	3	11
572 Rebekka	2013 November 10–15	32	4	31	−8	1.08	4	4
678 Fredegundis	2011 December 16–18	93	26	93	3	1.16	4	18
779 Nina	2012 October 16, 18	6	31	19	26	1.26	3/1	82
785 Zwetana	2013 March 5–20	165	32	154	23	1.21	12	21

Transmitter power was between 550 and 900 kW for all targets.
RA, DEC and λ, β (ecliptic) indicate the asteroid position (J2000) at center of observation window.
Dist is the Earth–asteroid distance in AU.
Total runs is the number of transmit-receive cycles.
OC SNR is the SNR of the optimally filtered weighted sum of all OC runs.

terrestrial and lunar pyroxenes," and 0.9 μm as with Frigga. Rivkin et al. (2000) report the existence of a 3 μm absorption feature and place Undina in the W-class.

We observed Undina on 11–14 November 2011 (Table 1) and obtained four runs with a total SNR of 25 (Fig. 3). We measured $B_{ZC} = 150 \pm 20$ Hz, constraining $D_{max} > 86$ km. No pole or shape has been reported for Undina. Assuming our adopted diameter, our bandwidth suggests a sub-radar latitude (observational aspect) of 45° ± 10°.

We measured an OC radar cross-section of $\sigma_{OC} = 4540 \pm 1200$ km^2 (Table 2), leading to a radar albedo $\hat{\sigma}_{OC} = 0.38 \pm 0.09$, suggesting a very high metal content. At some rotation phases, we measured radar albedos as high as 0.47. We measured an average circular polarization ratio of $\mu_c = 0.14 \pm 0.15$ with significant variation from run to run.

Three of our four radar runs on Undina show bifurcated echoes (runs #1, #2, and #4). Run #1 is nearly 180° in rotation from runs #2 and 4, suggesting the bifurcation is due to a contact binary structure and not simply a large concavity. Run #3 is at roughly the same rotation longitude as run #1, but does not show clear evidence of bifurcation; however, it has the lowest SNR of all the runs.

Reported lightcurves of Undina have relatively low amplitudes of Δmag ~ 0.17 (Warner et al., 2009a). This is generally thought to be inconsistent with a contact binary structure unless viewed at high latitudes, consistent with our speculation of $\delta = 45° \pm 10°$. We (BW) acquired new lightcurves during this observing window to confirm Undina's period and look for evidence of bifurcation; however, this aspect was similar to those previous and our amplitude was like-wise small, Δmag ~ 0.2. Shape modeling with existing lightcurves gave ill-defined solutions. We made additional lightcurve observations at the opposition of April 2014 – thought to be at a more equatorial aspect – but continued to see only modest lightcurve amplitudes. Unfortunately, that opposition was not within Arecibo's observation window.

3.3. (110) Lydia

Lydia has reported diameters of $D_{eff} = 86 \pm 2$ km (IRAS), 89 ± 6 km (WISE), and 83 ± 1 km (AKARI) and associated optical albedos of $p_v = 0.18 \pm 0.01$, 0.17 ± 0.04, and 0.20 ± 0.01 respectively. Durech et al. (2007) measure a rotation period of $P = 10.92580$ h and derive a convex shape model from 26 lightcurve observations over four oppositions. They report possible rotation poles of (λ, β) (331°, −61°) and (149°, −55°) and aspect ratios of $a/b \sim 1.1$ and $a/c \sim 1.5$. Using additional lightcurves, Warner et al. (2009b) obtained slightly different poles at (345°, −51°) and (164°, −43°) and report a less flattened aspect ratio of $a/c \sim 1.2$. Both sets of reported poles have radial uncertainties of 15°. Depending on the assumed pole, IRAS and WISE observed Lydia at sub-observer latitudes of between 25° and 45°.

Originally classified as a Tholen X-type, Lydia's albedo places it in the Tholen M-class. Rivkin et al. (2000) observed a 3-μm absorption feature and revised this designation to W-class. Optical polarimetry (Lupishko and Belskaya, 1989) and visible and near-infrared spectroscopy of Lydia (Hardersen et al., 2005, 2011; Ockert-Bell et al., 2010) suggest the presence of iron-poor orthopyroxenes on the surface.

In 2008, we first observed Lydia with the Arecibo radar, obtaining nine runs with a combined SNR of 10 (Shepard et al., 2010). We measured a bandwidth $B_{ZC} = 190 \pm 30$ Hz, constraining $D_{max} > 75$ km, an OC radar cross-section of $\sigma_{OC} = 1230 \pm 300$ km^2, and a polarization ratio of $\mu_c = 0.02 \pm 0.02$, suggesting a very smooth near-surface. At the time, we assumed $D_{eff} = 88 \pm 8$ km leading to a radar albedo estimate of $\hat{\sigma}_{OC} = 0.20 \pm 0.05$. At one rotation phase, we observed a strongly bifurcated echo, suggesting a complex shape or possible contact binary structure. Using only the stronger bifurcated echo, we obtained a radar albedo of $\hat{\sigma}_{OC} = 0.38 \pm 0.05$, suggesting a high metal content, at least at that orientation.

We re-observed Lydia from 15 to 18 October 2012 and obtained 7 runs with a combined SNR of 40 (Fig. 4). We measured a bandwidth of $B_{ZC} = 160 + 30/-0$ Hz, an OC radar cross-section of $\sigma_{OC} = 1976 \pm 500$ km^2, and a polarization ratio of $\mu_c = 0.06 \pm 0.03$. For these data, we estimate a radar albedo of $\hat{\sigma}_{OC} = 0.34 \pm 0.08$, with one run (#6, Table 2) giving an albedo of $\hat{\sigma}_{OC} = 0.48 \pm 0.12$. All of these runs support a high metal composition for Lydia.

Combining bandwidth data from 2008 and 2012 with the position of Lydia during these observations, we can place joint constraints on size and pole position. In Fig. 5 we plot contours of χ^2 consistent with both bandwidths and positions assuming a maximum diameter of 90 km along with the previously published poles (Durech et al. are triangles, Warner et al. are diamonds; both have dashed uncertainty circles of ±15°). Solutions larger than this are increasingly inconsistent with the published poles. The Warner et al. solutions are slightly better than the Durech et al. solutions, with the pole at (345°, −51°) having the lowest overall χ^2 value. Given these constraints and the Warner et al. estimates of aspect ratio, we adopt a new size estimate $D_{max} = 90$ km, leading to

Table 2
CW radar properties of individual targets.

Asteroid	Date	Time UT	SNR	ϕ (°)	B (Hz)	σ_{OC} (km^2)	μ_c
77 Frigga	2011 December 17	06:43	7	303 ± 40	206	750	0.00
	2012 January 26	03:26	9	0	125	523	0.00
	2012 January 26	04:15	8	33	125	596	0.00
	2012 January 26	05:04	9	65	125	609	0.20
	2012 January 27	03:23	6	237	130	447	0.26
	2012 January 27	05:04	6	304	140	432	0.00
	2012 January 28	03:24	5	116	142	621	0.00
	2012 January 28	04:17	9	152	121	623	0.14
	2012 January 28	05:04	6	184	138	339	0.05
	Sum of dates	–	20	–	152 ± 20	530 ± 150	0.03 ± 0.05
92 Undina	2011 November 11	06:29	9	0	150	5322	0.07
	2011 November 12	05:47	16	166	146	5545	0.31
	2011 November 13	05:47	8	348	176	3346	0.31
	2011 November 14	05:41	15	168	145	4292	0.00
	Sum of dates	–	25	–	150 ± 20	4540 ± 1200	0.14 ± 0.15
110 Lydia	2012 October 15	05:28	10	0	110	989	0.00
	2012 October 16	05:11	15	61	180	2122	0.04
	2012 October 16	06:05	14	91	160	1458	0.19
	2012 October 17	05:18	10	136	180	1279	0.40
	2012 October 17	06:12	21	165	190	2918	0.00
	2012 October 18	04:52	20	192	160	2781	0.00
	2012 October 18	05:46	23	222	130	2388	0.02
	Sum of dates	–	40	–	200 ± 30	1980 ± 500	0.06 ± 0.03
161 Athor	2013 November 13	03:59	5	0	–	–	–
	2013 November 13	04:46	5	38	–	–	–
	2013 November 14	03:28	7	81	–	–	–
	Sum of dates	–	10	–	200 ± 60	335 ± 100	0.32 ± 0.06
201 Penelope	2011 November 11	05:18	7	0	217	1647	0.00
	2011 November 14	04:30	15	0	283	2114	0.00
	Sum of dates	–	16	0	310 ± 50	2020 ± 500	0.00 ± 0.05
261 Prymno	2011 November 19	06:16	5	0	117	406	0.20
	2011 December 14	04:16	9	265	176	505	0.16
	2011 December 16	04:08	14	257	133	603	0.23
	2011 December 16	04:52	9	290	163	366	0.04
	Sum of dates	–	19	–	160 ± 30	480 ± 120	0.20 ± 0.05
359 Georgia	2013 October 15	03:05	6	0	284	423	0.09
	2013 October 15	03:53	6	51	235	500	0.42
	2013 October 17	02:54	6	290	235	488	0.06
	Sum of dates	–	10	–	227 ± 40	460 ± 120	0.16 ± 0.06
413 Edburga	2011 November 12	06:37	10	0	64	282	0.02
	2011 November 13	06:50	8	193	70	321	0.20
	2011 November 14	06:30	11	13	71	267	0.03
	Sum of dates	–	16	–	69 ± 10	280 ± 70	0.06 ± 0.06
441 Bathilde	2011 December 17	04:20	7	0	200	824	0.09
	2011 December 17	05:14	7	31	200	809	0.33
	2011 December 18	04:33	6	115	215	710	0.51
	Sum of dates	–	11	–	220 ± 20	780 ± 200	0.32 ± 0.07
572 Rebekka	2013 November 10	03:10	–	0	–	–	–
	2013 November 10	03:47	–	39	–	–	–
	2013 November 13	03:06	–	264	–	–	–
	2013 November 15	02:41	–	55	–	–	–
	Sum of dates	–	4	–	115 ± 60	42 ± 20	–
678 Fredegundis	2011 December 16	05:36	13	0	86	313	0.13
	2011 December 16	06:12	7	19	79	203	0.22
	2011 December 18	05:19	8	39	80	190	0.00
	2011 December 18	05:57	7	58	96	173	0.08
	Sum of dates	–	18	–	92 ± 15	220 ± 60	0.08 ± 0.06
779 Nina	2012 October 16	02:49	39	0	76	1237	0.10
	2012 October 16	03:31	50	23	70	1440	0.04
	2012 October 18	02:37	54	290	79	1725	0.03
	2012 October 18	03:21	dd	313		–	
	Sum of CW	–	82	–	74 ± 10	1470 ± 350	0.05 ± 0.02
785 Zwetana	2013 March 05	05:12	6	0	135	193	0.10
	2013 March 06	04:57	3	242	160	134	0.73

Table 2 (*continued*)

Asteroid	Date	Time UT	SNR	ϕ (°)	B (Hz)	σ_{OC} (km^2)	μ_c
	2013 March 06	05:31	5	265	150	279	0.00
	2013 March 07	04:05	16	100	140	456	0.00
	2013 March 07	04:44	9	127	160	291	0.18
	2013 March 07	05:22	7	152	110	238	0.08
	2013 March 08	03:55	7	346	170	253	0.02
	2013 March 08	04:35	4	12	150	143	0.27
	2013 March 08	05:14	5	39	90	151	0.90
	2013 March 18	03:09	7	319	100	144	0.47
	2013 March 18	03:51	4	347	100	112	0.00
	2013 March 20	03:17	7	109	170	249	0.38
	Sum of dates	–	21	–	170 ± 20	230 ± 60	0.20 ± 0.05

Values in the "Sum of Dates" are based on the weighted sum of all runs.
Time and date are the mid-epochs of acquisition (UT).
ϕ is rotation phase starting arbitrarily from the receipt of the first run (degrees) except 77 Frigga (see Fig. 1 for details).
B is zero-crossing bandwidth (Hz) for data smoothed in frequency (see text for specifics).
σ_{OC} is the OC radar cross-section (km^2), and μ_c is the polarization ratio.
Uncertainties in radar cross section are at least 25%.
Uncertainties in the polarization ratio for individual runs vary widely with SNR. We list only the uncertainty for the sum of runs.
We only list total properties for 161 Athor or 572 Rebekka because SNR was too low for individual runs.

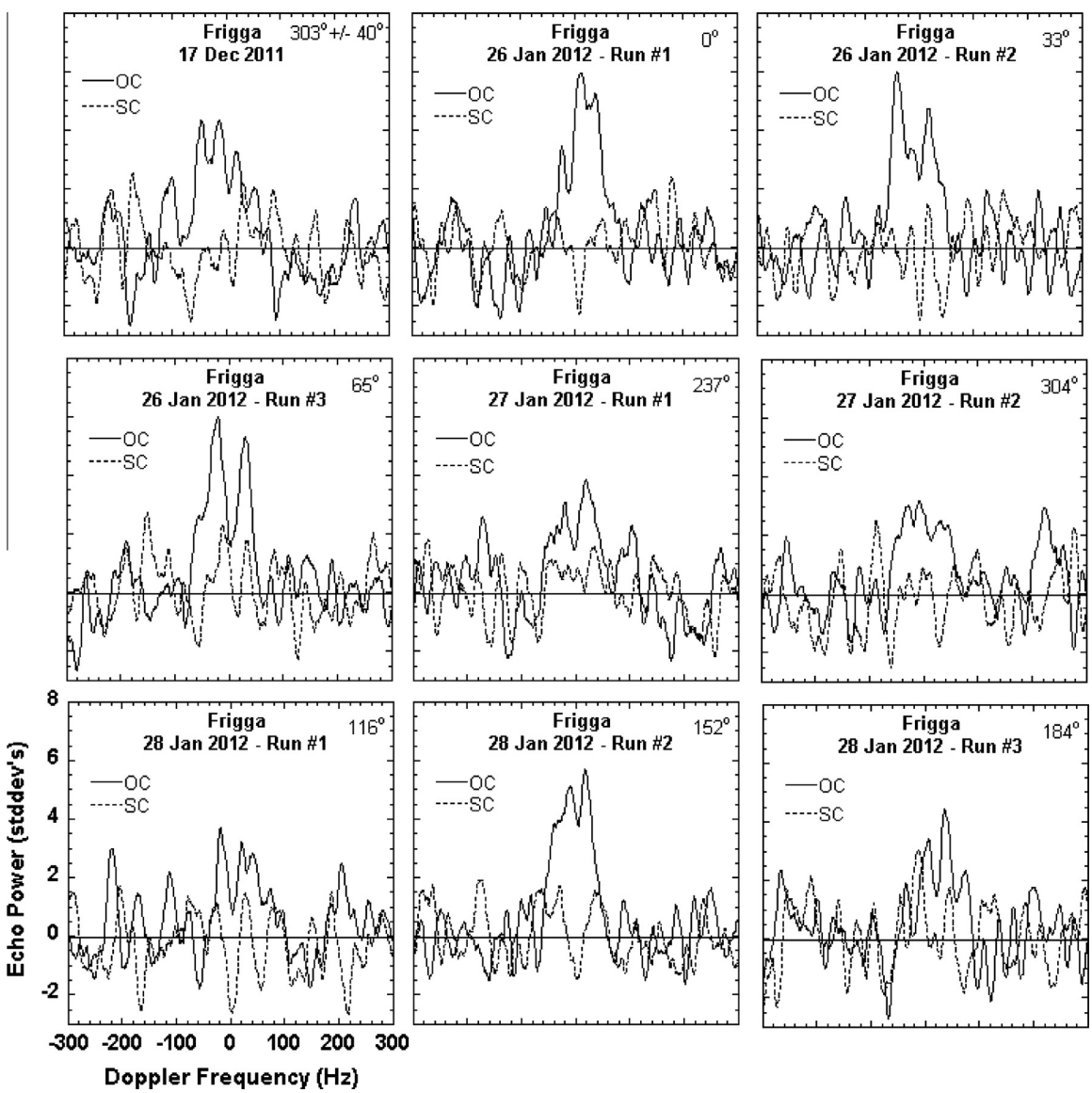

Fig. 1. CW spectra of 77 Frigga, smoothed to 20 Hz effective frequency resolution. Rotation is arbitrarily set to 0 at first run on 26 December 2012. The rotation phase on 17 December 2011 is uncertain by 40° because of uncertainty in its rotation period over the forty-day separation from the other runs and its plane-of-sky-motion.

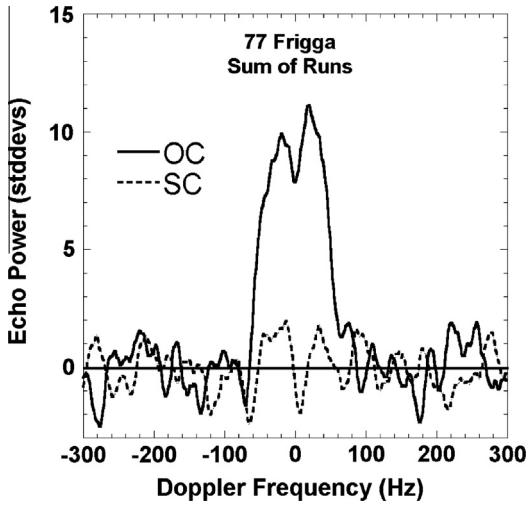

Fig. 2. Sum of all runs of 77 Frigga, smoothed to 20 Hz effective frequency resolution.

D_{eff} = 82 ± 10 km which slightly increases the overall radar albedo to $\hat{\sigma}_{OC} = 0.37 \pm 0.10$ and optical albedo p_v = 0.20 ± 0.02.

Radar run #6 showed a strongly bifurcated echo, consistent with our observations in 2008. To look for more evidence of a bifurcation, we first obtained a near-simultaneous lightcurve (BW). This showed a low amplitude, Δm = 0.2, inconsistent with the elongation that might be expected for a contact binary asteroid.

We also examined Lydia on four epochs from Keck AO imaging; one from 2002 (Merline et al., unpublished), plus three during the few weeks following our October 2012 radar observations. We attempted to time the latter two of these epochs to be most favorable for observing the suspected binary. Although some elongation (about 1.5×) was observed, no binary or contact binary structure was evident. At present, the radar, lightcurve, and AO data sets appear to be inconsistent with one another.

3.4. (161) Athor

Athor has reported diameters of 44.2 ± 3.3 km (IRAS) and 40.8 ± 0.5 km (AKARI), and associated optical albedos of 0.20 ± 0.03 and 0.23 ± 0.01, respectively. We adopt D_{eff} = 43 ± 4 km and p_v = 0.21 ± 0.02. Its rotation period is 7.280 h (Durech et al., 2010). Durech et al. have also computed a lightcurve derived shape model and two potential spin poles at (λ, β) (350°, −6°) and (170°, 4°). A 2002 occultation provides a diameter of 47 km, consistent with the IRAS and our adopted value (Dunham et al., 2014). Rivkin et al. (2000) found no evidence for a 3 μm absorption feature.

We observed Athor on 13–14 November 2013, obtaining three runs with a total SNR of 10 (Table 1). The weighted sum of all runs provided a bandwidth of 200 ± 60 Hz, a radar cross-section of 335 ± 100 km^2 and a polarization ratio of 0.32 ± 0.06 (Fig. 6, Table 2). Using the IRAS diameter and published poles, we expected a B_{max} = 152 Hz; our observations are therefore consistent with both the published size and either published pole. Our measured radar cross-section leads to an estimate of radar albedo of $\hat{\sigma}_{OC} = 0.22 \pm 0.06$. This is consistent with the majority of the other M-class asteroids we have measured, but is not consistent with a composition dominated by metal. Our polarization ratio implies a moderately rough near surface.

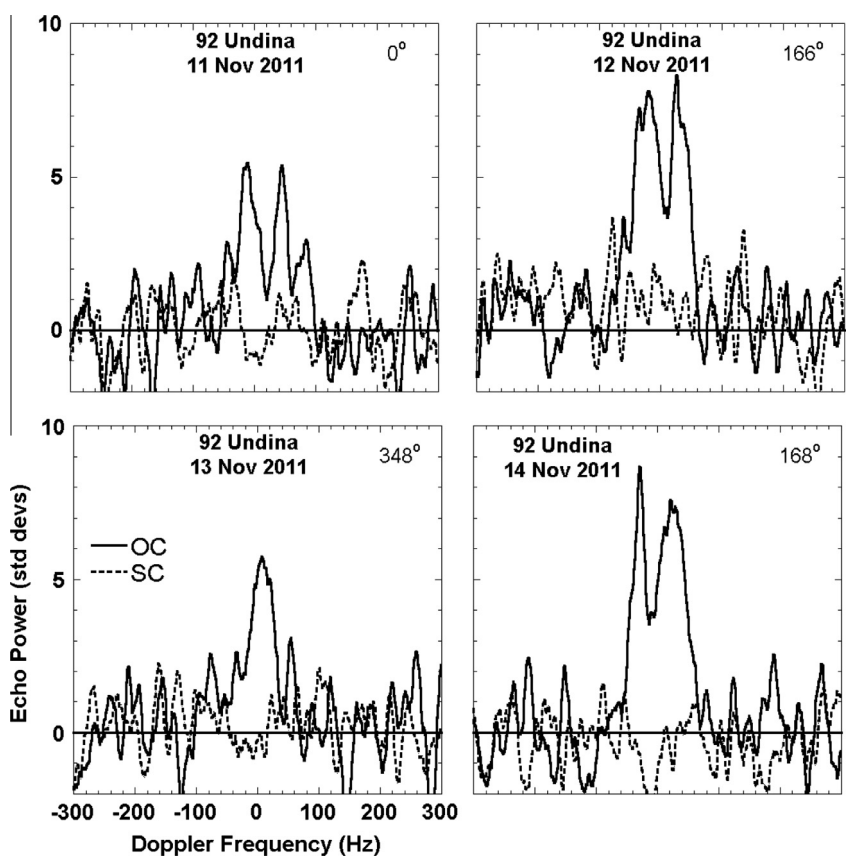

Fig. 3. Individual CW spectra of 92 Undina, smoothed to 15 Hz effective frequency resolution. Rotational phase is indicated and arbitrarily set to 0° for the first run.

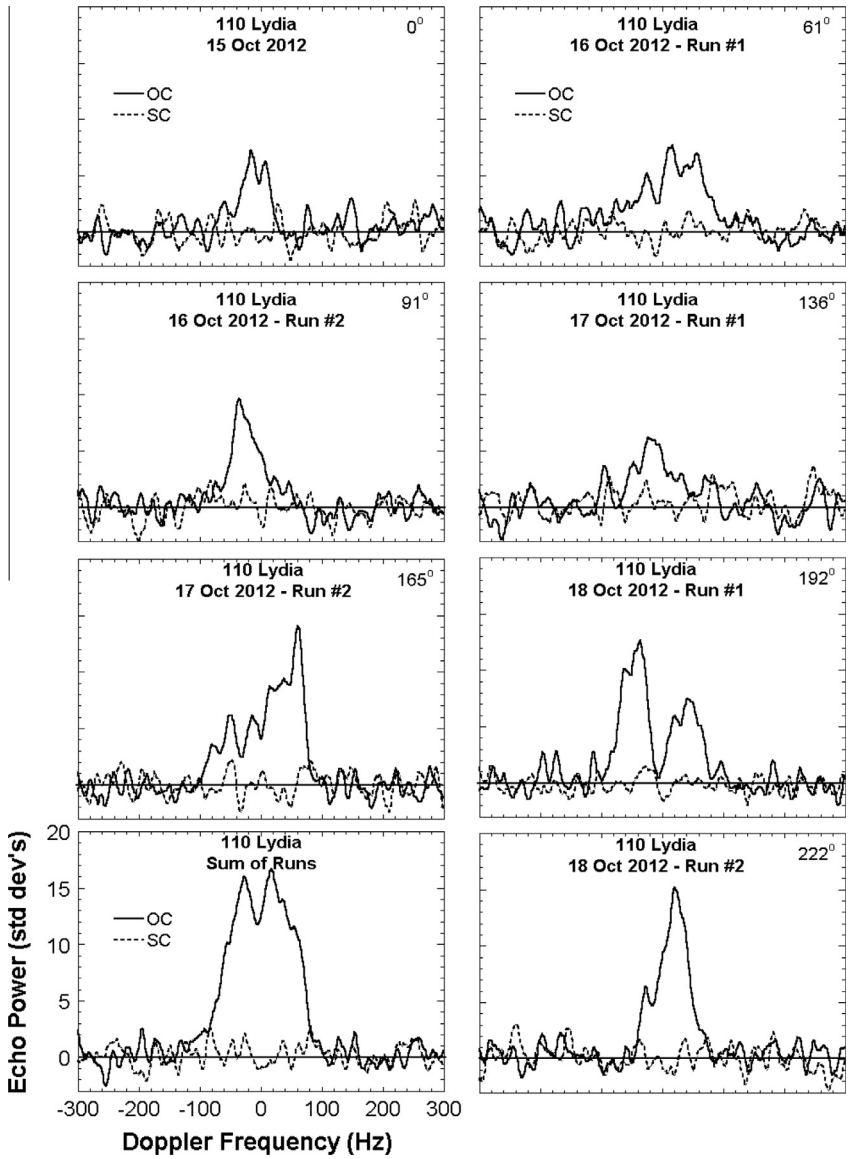

Fig. 4. CW spectra of 110 Lydia smoothed to 15 Hz effective frequency. The bottom image is the sum of all CW spectra. Rotational phase is indicated and arbitrarily set to 0° for the first run.

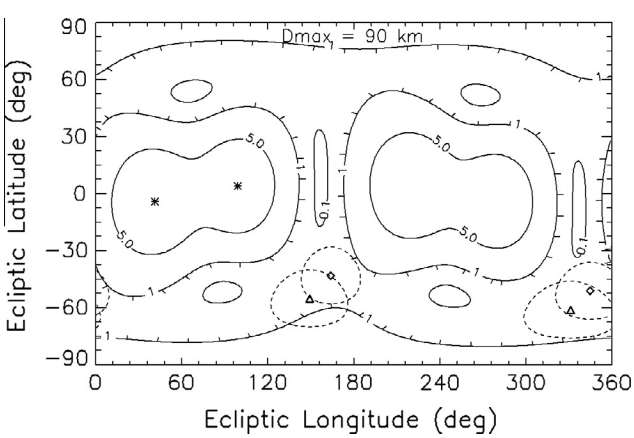

Fig. 5. χ^2 contour plot of pole solutions for Lydia assuming D_{max} = 90 km, the radar bandwidths and positions (shown as asterisks) at the time of the radar observations in 2008 and 2012. Triangles are poles according to Durech et al. (2007); diamonds are poles from Warner et al. (2009b). Uncertainty in pole positions is shown with dashed circles, ±15°.

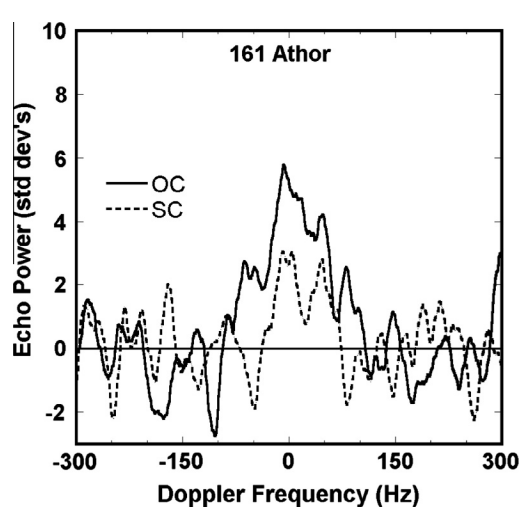

Fig. 6. Sum of CW spectra of 161 Athor, smoothed to 20 Hz effective frequency.

3.5. (201) Penelope

Penelope has estimated diameters of $D_{eff} = 68 \pm 4$ km (IRAS), 88 ± 3 km (WISE), and 66 ± 1 km (AKARI) with associated optical albedos of $p_v = 0.16 \pm 0.02$, 0.10 ± 0.01, and 0.18 ± 0.01, respectively. The AKARI diameter is similar to the IRAS value, but the WISE diameter is significantly higher.

Based on an analysis of multiple lightcurve, Torppa et al. (2003) find a rotation period of $P = 3.7474$ h and derive a shape model with aspect ratios of $a/b = 1.5$ and $b/c = 1.1$, and two possible rotational poles at (λ, β) (84°, −15°) and (262°, −1°). They also note hints of a contact binary structure in Penelope's lightcurves.

Hanus et al. (2013) use adaptive optics and lightcurve shape modeling above to estimate an equivalent diameter of $D_{eq} = 85 \pm 8$ km, consistent with the larger WISE diameter, and reject the second rotational pole. According to the time of their observations, the Hanus et al. (2013) AO observations were at a viewing aspect nearly pole on to the southern hemisphere ($\lambda = 245°$, $\beta = 9°$). Thus, this larger diameter is consistent with the largest areal aspect of Penelope.

According to the Minor Planet Center, the WISE observations of Penelope were made 28 February to 1 March 2010 (251°, 6°) and 26–27 August 2010 (248°, 6°). Assuming the Hanus et al. pole, these observations also occurred at a near polar aspect of (sub-observer latitude 74°) and should therefore also correspond with the largest areal aspect of Penelope.

According to the IRAS supplement (Tedesco et al., 2002), however, the IRAS observations of Penelope were made at a viewing aspect within 10° of an equatorial aspect ($\lambda = 183°$, $\beta = 4°$). The AKARI observations were made on 2–3 November 2006 (F. Usui, personal communication) when Penelope was at (310°, 0°); this corresponds to a mid-latitude viewing aspect (42°). The aspects of both IRAS and AKARI are therefore consistent with viewing Penelope's smaller dimensions and explaining their smaller reported diameters.

Using the information from the above sources, a good working model for Penelope's size and shape is a triaxial ellipsoid of dimensions 105 km × 72 km × 62 km. At polar aspects, it would have an area equivalent to an effective diameter of $D_{eff} = 87$ km, consistent with the AO and WISE diameters. At equatorial aspects, its projected area would be equivalent to $D_{eff} = 67$ km, consistent with the IRAS and AKARI diameters. This model gives $D_{eff} = 78 \pm 4$ km (assuming 5% uncertainty) and, given Penelope's absolute magnitude of $H = 8.43$, an estimated optical albedo of $p_v = 0.12 \pm 0.01$.

Hardersen et al. (2005) found evidence of orthopyroxenes in Penelope's near-infrared spectrum, but follow-up work by Hardersen et al. (2011) found no absorption features. Rivkin et al. (1995) identified a 3-μm feature in Penelope's spectrum and place it in their W-class. This observation is consistent with the inference of phyllosilicates from a 0.43 μm absorption feature reported by Busarev (1998). However, there has been no report of phyllosilicate absorption features in other surveys.

We observed Penelope at Arecibo on 11 and 14 November 2011 (Table 1), obtaining two runs with a total SNR of 16. The runs were taken at identical rotation phases and therefore represent the view of one side of Penelope. Our radar echoes show a significant dip in power near 0 Hz, suggesting a large concavity at this rotational aspect or a bifurcated structure. The weighted sum of both runs has a bandwidth $B = 310 \pm 50$ Hz (Fig. 7, Table 2), constraining $D_{max} > 42$ km for an equatorial aspect. Using the published pole and Penelope's position at the time of our observations, however, we expect a sub-radar latitude of 53°. If we adopt this aspect, our observations constrain $D_{max} \geqslant 70$ km, consistent with the ellipsoid model presented above.

We measured a total OC cross-section of $\sigma_{OC} = 2018 \pm 500$ km^2. Using the sky projection mode for asteroid shape models available at the DAMIT website (Durech et al., 2010) and our ellipsoid model, the apparent area of Penelope at the time of our observations gives an equivalent diameter of $D_{eff} = 80$ km, leading to a radar albedo estimate $\hat{\sigma}_{OC} = 0.40 \pm 0.10$, consistent with a composition dominated by metal. We measured a polarization ratio $\mu_c = 0.00 \pm 0.05$, indicative of a very smooth near-surface.

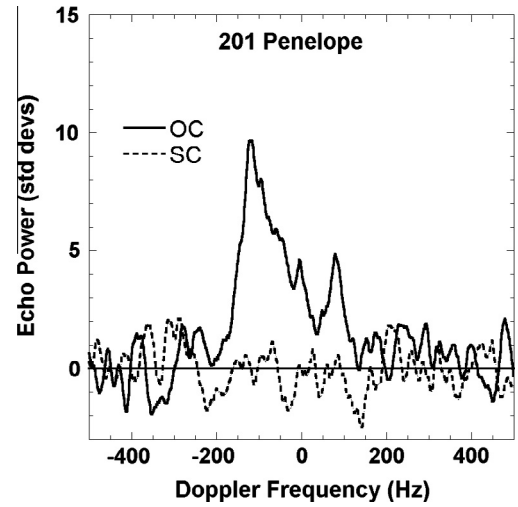

Fig. 7. Sum of CW spectra of 201 Penelope, smoothed to 25 Hz effective frequency.

3.6. (261) Prymno

Prymno has estimated diameters of $D_{eff} = 51 \pm 1.3$ km (IRAS), 54.2 ± 1.4 km (WISE), and 44.7 ± 0.5 km (AKARI) and associated optical albedos of $p_v = 0.11 \pm 0.01$, 0.10 ± 0.03, and 0.15 ± 0.01 respectively. We adopt $D_{eff} = 50 \pm 5$ km and $p_v = 0.11 \pm 0.02$. Lightcurves give a rotation period of $P = 8.002$ h, a nearly perfect 3:1 commensurability with Earth's rotation (Warner et al., 2009a). Prymno is classified as a Tholen B-class, but X in the Bus and Binzel (2002) system. Because of this and its moderate albedo, we included it in this survey. Observations by Howell et al. (in preparation) show no evidence of a 3 μm absorption feature.

We observed Prymno once on 19 November 2011 and three times between 14 and 16 December 2011 at Arecibo (Table 1). Our radar observations consist of four runs with a total SNR of 19 at an effective frequency of 105 Hz (Table 2). Based on the weighted sum of all runs, we estimate $B_{ZC} = 160 \pm 30$ Hz, constraining $D_{max} > 46$ km. Assuming our adopted diameter, this bandwidth is consistent with an equatorial viewing aspect (Fig. 8). We measured a total OC cross-section of $\sigma_{OC} = 477 \pm 120$ km^2, leading to a radar albedo estimate $\hat{\sigma}_{OC} = 0.24 \pm 0.06$. This is consistent with a significant metal content, but not with a composition dominated by metal. We measured a polarization ratio $\mu_c = 0.20 \pm 0.05$, indicative of a moderately rough near-surface.

3.7. (359) Georgia

Georgia has reported diameters of 43.9 ± 4.2 km (IRAS) and 50.8 ± 0.6 km (AKARI) and associated optical albedos of 0.26 ± 0.06 and 0.20 ± 0.01, respectively. We adopt $D_{eff} = 48 \pm 4$ km and $p_v = 0.23 \pm 0.02$. Its rotation period is 5.537 h. It is classified as an X in the Bus and Binzel system and was classified as CX in the Tholen taxonomy. Its geometric albedo places it in the Tholen M-class. Rivkin et al. (2000) found no evidence for a 3 μm absorption feature. Little else is known about Georgia.

We observed Georgia on 15 and 17 October 2012, obtaining three CW runs with a total SNR of 10 (Fig. 9) We measured an echo

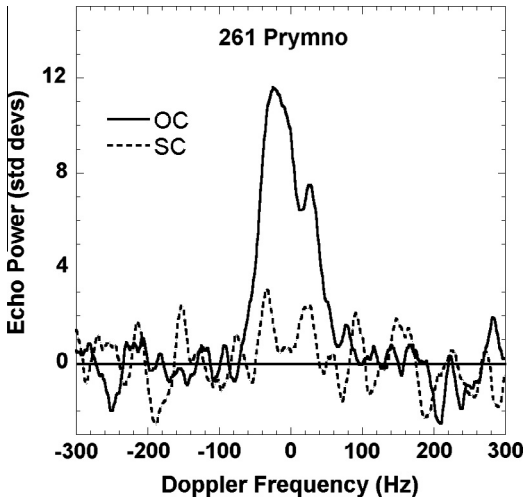

Fig. 8. Sum of CW spectra of 261 Prymno, smoothed to 20 Hz effective frequency.

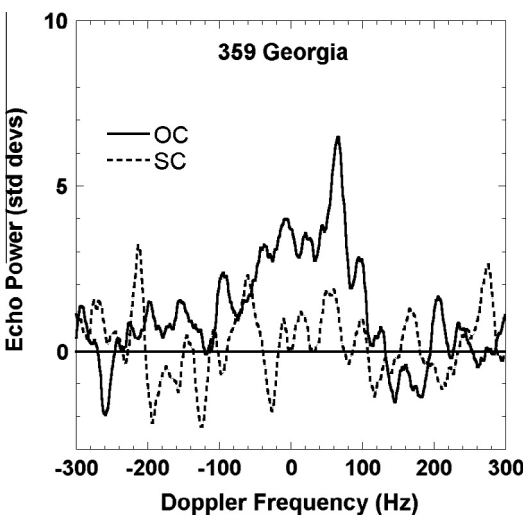

Fig. 9. Sum of CW spectra of 359 Georgia, smoothed to 20 Hz effective frequency.

bandwidth of $B_{ZC} = 227 \pm 30$ Hz, constraining $D_{max} > 45$ km; given the reported rotation rate and IRAS diameter, these observations are consistent with an equatorial view. Given Georgia's observed radar cross-section of 464 ± 120 km^2, we estimate a radar albedo of $\hat{\sigma}_{OC} = 0.26 \pm 0.08$. Georgia's polarization ratio is $\mu_c = 0.16 \pm 0.06$ which indicates a moderately smooth near-surface.

3.8. (413) Edburga

Edburga has estimated diameters of $D_{eff} = 32 \pm 3$ km (IRAS) and 34.2 ± 0.6 km (AKARI) and associated optical albedos of $p_v = 0.15 \pm 0.03$ and 0.13 ± 0.01, respectively. It has two separate entries in the preliminary WISE diameters: the first gives $D_{eff} = 30.7 \pm 0.3$ km with $p_v = 0.16 \pm 0.03$ and the second gives 40.1 ± 0.5 and $p_v = 0.09 \pm 0.01$.

Edburga is classified as an M in the Tholen and X in the Bus and Binzel systems. Observations by Howell et al. (in preparation) show the presence of a 3 μm absorption feature, placing Edburga in the W-class.

Using numerous lightcurves, Hanus et al. (2011) report a rotation period of $P = 15.772$, a rotational pole at (λ, β) (202°, −45°), and aspect ratios of $a/b \sim 1.6$ and $b/c \sim 1.2$. If we adopt the IRAS and AKARI effective diameters and the Hanus et al. aspect ratios, Edburga can be modeled as a triaxial ellipsoid with dimensions of $46 \times 29 \times 25$ km, $D_{eff} = 32 \pm 3$ km, and $p_v = 0.15 \pm 0.02$.

WISE observed Edburga on 10–11 February 2010 (231°, 19°) and 27 July 2010 (218°, 14°). Assuming the Hanus et al. pole, WISE observed it at sub-observer latitudes of 21° and 29°. The wise observations on both dates occurred over a ~24 h period, so no single rotation phase can be attributed to each diameter. However, the two disparate diameters of 31 km and 40 km might be explained as either different rotation phases dominating the two sets of observations or perhaps due to the ~10° difference in viewing aspects.

We observed Edburga between 12 and 14 November 2011 (Table 1), obtaining three runs with a total SNR of 16 (Fig. 10, Table 2). Based on the weighted sum of all runs, we estimate $B_{ZC} = 69 \pm 10$ Hz, constraining $D_{max} \geqslant 39$ km. This is consistent with the modeled shape and an viewing aspect between 0° and 30° latitude and the Hanus et al. pole.

We measured a total OC cross section of $\sigma_{OC} = 281 \pm 70$ km^2, giving a radar albedo estimate of $\hat{\sigma}_{OC} = 0.35 \pm 0.09$ and suggesting a high metal content. We measured a polarization ratio $\mu_c = 0.06 \pm 0.06$ which suggests a smooth near-surface.

Edburga's echoes were consistently bimodal, suggesting a bifurcated structure. Runs #1 and #3 were at approximately the same rotational longitude (arbitrarily designated to be 0°) while run #2 was ~180° away in rotation. Using the sky-projection tool for asteroid shape models at the DAMIT website (Durech et al., 2010), our radar observation times correspond to broadside and equatorial aspects, consistent with expectations for a contact binary.

3.9. (441) Bathilde

Bathilde has estimated diameters of $D_{eff} = 70 \pm 3$ km (IRAS), 70.8 ± 2.9 km (WISE), and 59.4 ± 0.6 km (AKARI) and associated optical albedos of $p_v = 0.14 \pm 0.01$, 0.14 ± 0.03, and 0.20 ± 0.01, respectively. The AKARI derived diameter is considerably smaller than IRAS or WISE and we adopt $D_{eff} = 70 \pm 3$ km and $p_v = 0.14 \pm 0.02$. Bathilde has a rotation period of $P = 10.446$ h (Warner et al., 2009a). It is classified as a Tholen M-class and Xk in the Bus and Binzel system. No pole or shape has been reported.

Ockert-Bell et al. (2010) report a 0.9 μm pyroxene absorption, but Hardersen et al. (2005, 2011) report only featureless spectra.

We observed Bathilde on 17–18 December 2011 (Table 1) and obtained a total of 3 runs with a total SNR of 11 at an effective frequency of 210 Hz (Fig. 11). We measured $B_{ZC} = 220 \pm 20$ Hz. Including the uncertainties, our observations constrain Bathilde's maximum diameter to be $D_{max} > 75$ km. Based on its modest lightcurve amplitude (Table 3), we assume Bathilde to be approximately equant in shape. Our bandwidth is thus consistent with the upper limit of the IRAS diameter estimate and requires an equatorial viewing aspect.

We measured a total OC cross section of $\sigma_{OC} = 780 \pm 200$ km^2, leading to a radar albedo estimate $\hat{\sigma}_{OC} = 0.20 \pm 0.05$ (Table 2). While higher than the average main-belt asteroid, this is not consistent with a metal dominated composition. We measured a polarization ratio $\mu_c = 0.32 \pm 0.07$, indicative of a moderately rough near-surface.

3.10. (572) Rebekka

Tholen (1984) classified Rebekka as XCD (similar to featureless X, C, and D classes) while Bus and Binzel (2002) assign it to the C-class. Rebekka has reported diameters of 29.6 ± 3.3 km (IRAS) and 26.2 ± 0.4 km (AKARI) and associated optical albedos of 0.085 ± 0.01 and 0.11 ± 0.01, respectively. We adopt $D_{eff} = 27 \pm 3$ km and $p_v = 0.10 \pm 0.01$. Although its optical albedo is at the

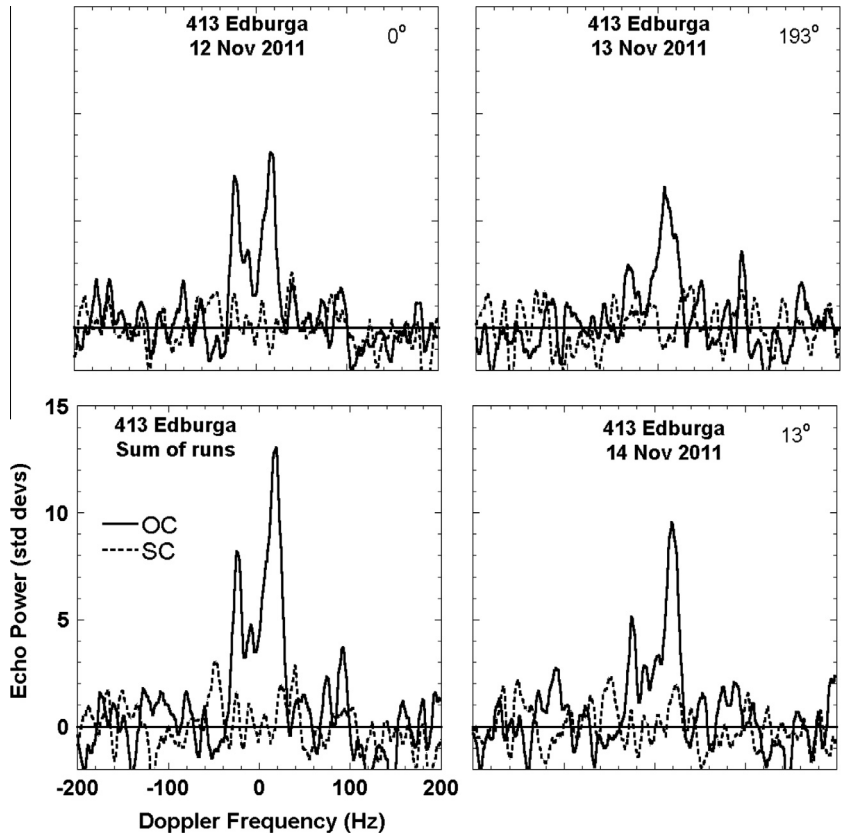

Fig. 10. Individual CW spectra of 413 Edburga, each smoothed to 10 Hz effective frequency and labeled with the rotation phase (arbitrarily set to 0 for the first run), and sum of runs.

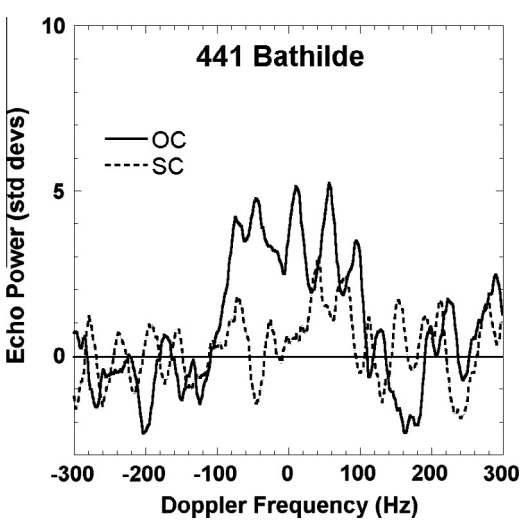

Fig. 11. Sum of CW spectra of 441 Bathilde, smoothed to 20 Hz effective frequency.

bottom edge of the M-class albedo cutoff, it is included in the M-asteroids investigated by Rivkin et al. (1995), Belskaya and Lagerkvist (1996), Ockert-Bell et al. (2008), and Hardersen et al. (2011). We include it here for completeness.

Rebekka's rotation period is 5.6497 h (Durech et al., 2010). Durech et al. have also computed a lightcurve derived shape model and two potential spin poles at (λ, β) (1°, 54°) and (158°, 39°). Rivkin et al. (2000) found no evidence for a 3 μm absorption feature.

We observed Rebekka on 10–15 November 2013, obtaining four runs with a total SNR of 4.3, a minimal detection (Table 1). The weighted sum of all runs provided a bandwidth of 115 ± 60 Hz and a radar cross-section of 42 ± 25 km^2 (Fig. 12, Table 2). We measured a polarization ratio of 0.6, but the SNR for the SC echo is dominated by noise and this estimate is of little value. Using the adopted diameter and published poles, we expect a maximum bandwidth of B_{max} = 147 Hz; our observations are therefore consistent with both the published size and either published pole. Our measured radar cross-section leads to an estimate of radar albedo of $\hat{\sigma}_{OC} = 0.06 \pm 0.03$, the lowest value measured for any potential M-class asteroid except possibly 83 Beatrix. Based on this admittedly weak data set, we find that Rebekka, like 83 Beatrix, is probably a primitive object with a very low surface bulk density and little to no metal content.

3.11. (678) Fredegundis

Fredegundis has estimated diameters of D_{eff} = 42 ± 4 km (IRAS), 42.0 ± 2.4 km (WISE), and 42.1 ± 0.8 km (AKARI) and associated optical albedos of p_v = 0.25 ± 0.03, 0.33 ± 0.08, and 0.25 ± 0.01 respectively. The somewhat arbitrary optical albedo boundary separating M- and E-class asteroids is 0.3. Given the radar evidence presented below, we exclude the E-classification and adopt D_{eff} = 42 ± 3 km and p_v = 0.25 ± 0.02.

Stephens et al. (2008) measured a rotational period of P = 11.6201 h. Classified as an X in the Bus and Binzel system, its optical albedo places it in the Tholen M-class. Ockert-Bell et al. (2010) report a 0.9 μm pyroxene absorption feature. Observations by Howell et al. (in preparation) show the presence of a 3 μm absorption feature, moving Fredegundis into the W-class.

We (Shepard et al., 2010) originally observed Fredegundis at Arecibo between 10 and 17 January 2008, obtaining 10 runs with a total SNR of 15 and a bandwidth of B_{ZC} = 100 ± 20 Hz. During that encounter, we measured a total OC cross-section of

Table 3
M- and X-class asteroids observed by radar.

Asteroid	D_{eff} (km)	p_v	P (h)	$\hat{\sigma}_{OC}$	μ_c	Δm	Tholen	Bus-DeMeo	Rivkin M/W	Radar	Bifur Echo?
16 Psyche	186 ± 30	0.23 ± 0.05	4.196	0.42 ± 0.10	0.06 ± 0.02	0.03–0.42	M	Xk	M	Mm	
21 Lutetia	100 ± 11	0.20 ± 0.03	8.172	0.24 ± 0.07	0.22 ± 0.05	0.08–0.25	M	Xc	W		
22 Kalliope	162 ± 3	0.14 ± 0.01	4.148	0.18 ± 0.05	0.07 ± 0.10	0.04–0.30	M	Xk	W		
69 Hesperia	110 ± 15	0.22 ± 0.03	5.655	0.45 ± 0.12	0.05 ± 0.05	0.12–0.20	M	X	W	Mm	
77 Frigga	68 ± 4	0.15 ± 0.01	9.012	0.14 ± 0.04	0.03 ± 0.05	0.07–0.19	MU	Xe	W		Y
83 Beatrix	81 ± 2	0.09 ± 0.01	10.16	0.07 ± 0.03	0.23 ± 0.11	0.18–0.27	X	X	–		
92 Undina	123 ± 6	0.26 ± 0.01	15.941	0.38 ± 0.09	0.14 ± 0.04	0.17	X	Xc	W	Mm	Y
97 Klotho	83 ± 5	0.23 ± 0.03	35.15	0.26 ± 0.05	0.24 ± 0.02	0.07–0.25	M	Xc	–		
110 Lydia	82 ± 8	0.20 ± 0.02	10.926	0.37 ± 0.10	0.06 ± 0.03	0.10–0.20	X	Xk	W	Mm	Y
129 Antigone	113 ± 12	0.21 ± 0.05	4.957	0.36 ± 0.09	0.14 ± 0.02	0.21–0.49	M	Xk	W	Mm	Y
135 Hertha	77 ± 7	0.14 ± 0.01	8.401	0.18 ± 0.05	0.10 ± 0.03	0.12–0.30	M	Xk	W		
161 Athor	43 ± 4	0.22 ± 0.03	7.280	0.22 ± 0.06	0.32 ± 0.06	0.1–0.27	M	Xc	M		
201 Penelope	78 ± 4	0.12 ± 0.01	3.747	0.40 ± 0.10	0.00 ± 0.05	0.15–0.73	M	X	W	Mm	Y
216 Kleopatra	124 ± 15	0.12 ± 0.02	5.385	0.60 ± 0.15	0.00 ± 0.04	0.13–1.18	M	X	M	Mm	Y
224 Oceana	62 ± 2	0.17 ± 0.01	9.388	0.25 ± 0.10	0.33 ± 0.06	0.10	M	Xc	–		
261 Prymno	50 ± 5	0.11 ± 0.02	8.002	0.24 ± 0.06	0.20 ± 0.05	0.17	B	X	W		
325 Heidelberga	76 ± 2	0.11 ± 0.01	6.737	0.17 ± 0.08	0.0 ± 0.1	0.20	M	–	–		
347 Pariana	51 ± 5	0.18 ± 0.02	4.053	0.36 ± 0.09	0.05 ± 0.03	0.09–0.42	M	Xk	–	Mm	
359 Georgia	48 ± 4	0.23 ± 0.06	5.537	0.26 ± 0.08	0.16 ± 0.06	0.22–0.54	CXM	X	M		
413 Edburga	32 ± 3	0.15 ± 0.02	15.773	0.35 ± 0.09	0.06 ± 0.06	0.46	M	X	W	Mm	Y
441 Bathilde	70 ± 3	0.14 ± 0.02	10.446	0.20 ± 0.05	0.32 ± 0.07	0.13	M	Xk	–		
497 Iva	40 ± 8	0.13 ± 0.03	4.620	0.24 ± 0.08	0.11 ± 0.03	0.38–0.50	M	Xk	M		
572 Rebekka	27 ± 3	0.10 ± 0.01	5.650	0.06 ± 0.03	No data	0.30	XDC	C	M		
678 Fredegundis	42 ± 3	0.25 ± 0.02	11.620	0.16 ± 0.04	0.03 ± 0.06	0.25	X	Xk	W		Y
758 Mancunia	85 ± 7	0.13 ± 0.02	12.738	0.55 ± 0.14	0.34 ± 0.03	0.15	X	Xk	M	Mm	Y
771 Libera	29 ± 2	0.13 ± 0.01	5.892	0.17 ± 0.04	0.37 ± 0.09	0.53–0.57	X	Xk	M		
779 Nina	77 ± 7	0.15 ± 0.02	11.186	0.32 ± 0.08	0.05 ± 0.02	0.25	X	Xk	W	Mm	Y
785 Zwetana	50 ± 2	0.12 ± 0.01	8.919	0.26 ± 0.07	0.17 ± 0.02	0.13–0.18	M	Cb	M		Y
796 Sarita	45 ± 2	0.20 ± 0.01	7.75	0.25 ± 0.10	No data	0.29	XD	S	M		

Notes. D_{eff} is asteroid effective diameter, p_v is visual albedo, P is rotation period, $\hat{\sigma}_{OC}$ is radar albedo, μ_c is circular polarization ratio, and Δm is the observed lightcurve amplitude from the Minor Planet Lightcurve Data File (Warner et al., 2009a; www.minorplanetcenter.net). Objects in bold were discussed in this paper; others in Shepard et al. (2008, 2010). The classifications listed are based on the following references: Tholen (Tholen, 1984), Bus-DeMeo (Bus and Binzel, 2002; DeMeo et al., 2009); Rivkin (Rivkin et al., 2000), radar (Shepard et al., 2010). Uncertainties are listed for all quantities except the rotation period, which is on the order of the last significant digit. Diameters and visual albedos are primarily from the IRAS data set (Tedesco et al., 2002) except where modified by others or our previous radar data (see text and Shepard et al., 2008, 2010 and references therein). The "Bifur Echo?" column notes whether the radar echo is bifurcated.

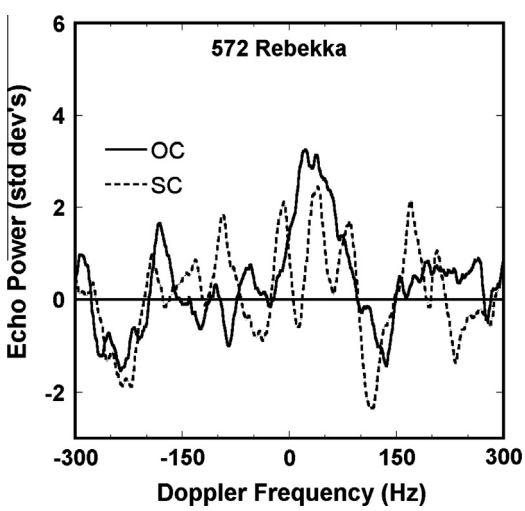

Fig. 12. Sum of CW spectra of 572 Rebekka, smoothed to 30 Hz effective frequency.

$\sigma_{OC} = 240 \pm 60$ km^2, leading to a radar albedo estimate $\hat{\sigma}_{OC} = 0.18 \pm 0.05$, and measured a polarization ratio $\mu_c = 0.03 \pm 0.06$. Benner et al. (2008) and Shepard et al. (2008) found that all known E-class asteroids have extremely high radar polarizations. Based on the observed polarization ratio of Fredegundis, we therefore exclude it as a possible E-class asteroid.

Our 2008 radar observation also showed evidence of a bifurcated radar echo in two runs, an indicator of a possibly bifurcated structure. Lightcurves taken at the same time (Stephens et al., 2008) were of only moderate amplitude ($\Delta m \sim 0.25$), but the shapes were consistent with a contact binary structure. Shape modeling of its lightcurves was unable to rule out non-contact binary structures.

We re-observed Fredegundis at Arecibo on 16 and 18 December 2011, specifically to look for additional evidence of bifurcated echoes (Fig. 13, Table 1). Fredegundis's position was only ~20° from the previous encounter, so we expected little change in bandwidth. We obtained four runs with a total SNR of 18 and measured a bandwidth of $B_{ZC} = 92 \pm 15$ Hz, consistent with our previous observations (Table 2). Our bandwidth observations constrain $D_{max} > 42$ km, consistent with the adopted diameter and an equatorial aspect if the shape is not elongate.

We measured a mean radar cross-section of $\sigma_{OC} = 220 \pm 80$ km^2, also consistent with the previous encounter. We did not see aspects with large increases in radar cross-section as we did in the 2008 observations, but our observing window (and the asteroid's nearly 12 h period) constrained our view to a 60° longitude swath. Applying our adopted diameter leads to a radar albedo of $\hat{\sigma}_{OC} = 0.16 \pm 0.04$.

Of our observations, only run #4 shows evidence of a bifurcated echo. The SNR is modest, but the shape is clearly evident. Without a pole and shape model, however, we cannot put this observation in context with those in 2008.

3.12. (779) Nina

Nina has estimated diameters of 76.6 ± 4 km (IRAS), 77.0 ± 6.6 km (WISE), and 81.3 ± 1.0 km (AKARI) with associated optical albedos of $p_v = 0.14 \pm 0.03$, 0.17 ± 0.06, and 0.13 ± 0.01 respectively; we adopt 77 ± 7 km and $p_v = 0.15 \pm 0.02$. Nina's rotation period is reported to be 11.186 h (Warner et al., 2009a). It is classified as an X in the Bus and Binzel system; with an optical

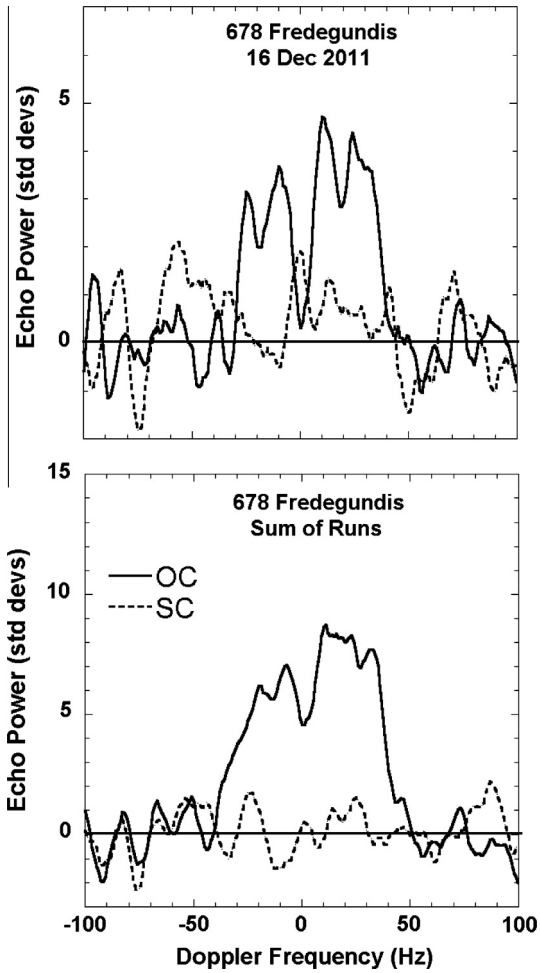

Fig. 13. CW spectra of 678 Fredegundis smoothed to 10 Hz effective frequency. Top image shows a bifurcated echo observed on 16 December 2011. The bottom image is the sum of all CW spectra.

albedo of $p_v = 0.16 \pm 0.03$ it is also classified as an M in the Tholen system.

Ockert-Bell et al. (2010) report 0.9 and 1.8 μm silicate absorption features in Nina's spectra. Observations by Howell et al. (in preparation) show the presence of a 3 μm feature, placing Nina in the W-class. Those data can also be fit with a thermal model and used to estimate a diameter and optical albedo. When this is done, they obtain a best fit diameter of 85 ± 6 km, an optical albedo of 0.16 ± 0.02, and a thermal inertia of $10 + 40/-5$ J m^{-2} K^{-1} s$^{-0.5}$. This diameter estimate is consistent with, but slightly larger than our adopted value.

We originally observed Nina in November 2008 and obtained three runs (Shepard et al., 2010). We measured a bandwidth of $B_{ZC} = 135 \pm 20$ Hz, constraining $D_{max} > 54$ km, a polarization ratio of $\mu_c = 0.16 \pm 0.08$, and, assuming the adopted diameter, a mean radar albedo of $\hat{\sigma}_{OC} = 0.16 \pm 0.04$. Although the mean radar albedo is not high, one of the three runs was perpendicular to the other two (which were at essentially the same rotation phase) and provided a radar albedo of $\hat{\sigma}_{OC} = 0.50 \pm 0.12$. We therefore classified Nina as an Mm-class. The high albedo run also displayed a bifurcated waveform, suggesting a complex shape and possibly a contact binary structure. However, the variations in bandwidth with rotation were modest and not consistent with an elongate object.

We re-observed Nina on 16 and 18 October 2012, obtaining two CW runs on the 16th and one CW run and one delay-Doppler image on the 18th (Fig. 14). The SNR during this encounter was 82 for the sum of the CW runs, nearly eight times higher than observed in 2008. We measured a bandwidth of $B_{ZC} = 70 \pm 5$ Hz, much narrower than in 2008. Our summed CW runs gave a radar cross-section of 1467 ± 350 km; assuming a diameter of 77 km leads to a radar albedo of $\hat{\sigma}_{OC} = 0.32 \pm 0.08$, consistent with the previous interpretation of a high-metal content. We measured a polarization ratio of $\mu_c = 0.05 \pm 0.02$, suggesting a macroscopically smooth surface.

Our CW run on 18 October displayed a bifurcated echo, similar to that observed in 2008 albeit at a much higher SNR. We obtained a delay-Doppler image (resolution of 3 km/pixel) of Nina some 50 min after the CW run, equivalent to a 25° rotation difference. That image (Fig. 15) shows two radar-bright regions separated in Doppler frequency as might be expected from the CW echo. However, the image does not support the interpretation of two independent lobes or a contact binary; instead, it appears to be a single, approximately equant object with two separated regions of high radar albedo. The overall radar albedo suggests these two regions are highly enriched in metal, flat with little regolith and favorably oriented to the Earth, or some combination of these.

From the delay-Doppler image, we measured a total delay-depth of 180 μs which corresponds to 27 km in radius. This gives a minimum estimate of 54 km for Nina's diameter which is considerably smaller than the 77 km diameter. However, this is not an unexpected result given the low SNR of the image data.

Our observations of Nina in 2008 and 2012 allow us to place tight constraints on its spin pole. In Fig. 16 we plot contours of χ^2 consistent with both bandwidths and positions assuming a maximum diameter of 90 km. Solutions with $D_{max} > 75$ km are relatively insensitive to the maximum diameter and give essentially the same pole solutions. Our best estimate of Nina's spin pole is (λ, β) (40, +25) or (220, −25), with uncertainties of +5°/−20 in longitude and ±20° in latitude.

3.13. (785) Zwetana

Zwetana has reported diameters of $D_{eff} = 49 \pm 2$ km (IRAS) and 50.7 ± 0.6 km (AKARI) and associated visual albedos $p_v = 0.12 \pm 0.01$ and 0.12 ± 0.01, respectively. We adopt $D_{eff} = 50 \pm 2$ km and $p_v = 0.12 \pm 0.01$. Its rotational period is $P = 8.8882$ h (Shepard et al., 2008). Ockert-Bell et al. (2010) report unusual absorption features at 0.6 and 1.7 μm, while Hardersen et al. (2005, 2011) report no near-infrared absorption features. Rivkin et al. (2000) report no observed 3 μm hydration feature in its spectrum. No pole or shape model for it has been published.

We (Shepard et al., 2008) observed Zwetana in April and May, 2005, and obtained 13 CW runs with a total SNR of 44. We observed a bandwidth of 161 ± 20 Hz, consistent with the adopted diameter and an equatorial aspect. Our observations showed radar albedo varying by a factor of six (0.1–0.6) with rotation, the largest variation of any asteroid. Repeat observations at the same rotation phases confirmed the large swings in radar albedo. Simultaneous lightcurves by us (Shepard et al., 2008), however, showed little variation and suggested a nearly equant object. Observations in the VISIR showed less than 1% variation with rotation, effectively ruling out a superficial compositional cause (Ockert-Bell et al., 2008).

Several possible interpretations of these large swings in radar albedo have been discussed. Perhaps there are large variations in regolith thickness; in areas where it is thin or missing, radar penetrates to the more coherent undersurface, enhancing the backscatter, while in areas where it is thick, the radar energy is absorbed (Shepard et al., 2008). Two other suggestions involve shape effects. In the first, we speculated that large-scale flat areas were favorably oriented during the 2005 encounter to enhance the backscatter (Shepard et al., 2008); in the latter, favorable shapes could deflect much of the radar energy in the forward scattering direction, greatly reducing the observed backscattering radar

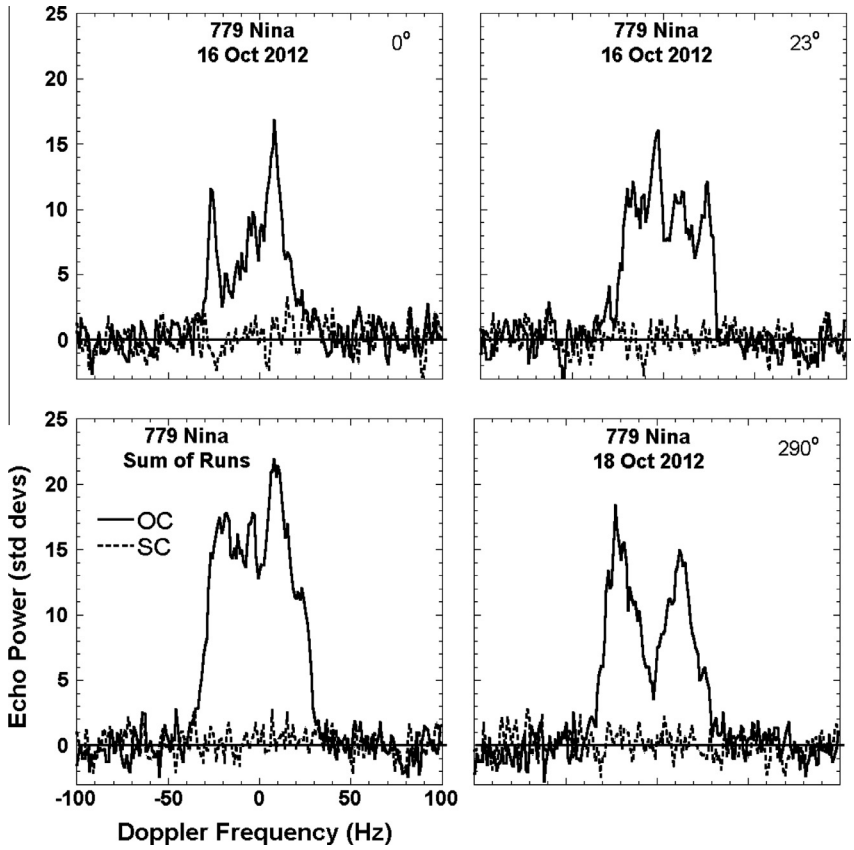

Fig. 14. Individual CW spectra of 779 Nina, each smoothed to 2 Hz effective frequency and labeled with the rotation phase (arbitrarily set to 0 for the first run), and sum of runs.

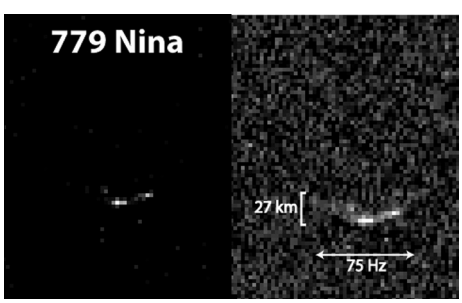

Fig. 15. Delay-Doppler image of 779 Nina. The image on the left is not stretched and shows two areas of high radar reflectivity that could give the bifurcated echo seen in the CW data. The image on the right is stretched and shows that the asteroid is not bifurcated. Bandwidth and minimum delay-depth are shown.

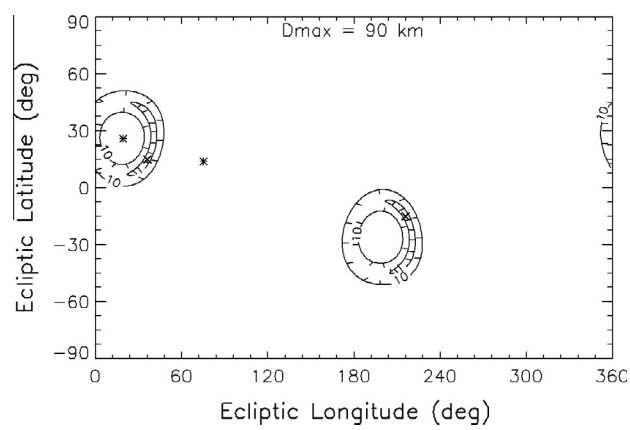

Fig. 16. χ^2 contour plot of pole solutions for Nina assuming D_{max} = 90 km, and the radar bandwidths and positions at the time of the radar observations in 2008 and 2012 (shown by a bold asterisk). The crescent shaped contours with those for χ^2 = 10 are for χ^2 = 1. The X's mark the minimum chi2.

albedo (Shepard et al., 2010). In the former case, the inherent reflectivity of Zwetana would be low to moderate (i.e. silicate dominated), while in the latter case, the inherent reflectivity could be high (i.e. metal dominated).

We observed Zwetana a second time from 5 to 20 March 2013, obtaining twelve (12) CW runs (Fig. 17, Table 1). During this encounter, Zwetana was 49° from our previous observations, giving us a different viewing aspect. Our summed runs had an SNR of 21 and a bandwidth of 170 ± 30 Hz, constraining D_{max} > 54 km. We obtained lightcurves during this encounter as well, observing a low lightcurve amplitude of $\Delta m \sim 0.2$, consistent with our previous observations and confirming that Zwetana is roughly equant in shape. All of our observations are consistent with the adopted diameter and modest elongation, and a near-equatorial aspect.

Combining bandwidth data from 2005 to 2013 with the position of Zwetana during these observations, we can place joint constraints on size and pole position. In Fig. 18 we plot contours of χ^2 consistent with both bandwidths and positions assuming an aspect ratio of $a/b \sim 1.1$ and maximum diameter of 55 km. The positions of Zwetana are marked by asterisks. Poles most consistent with our observations fall outside the χ^2 = 1 contour.

Zwetana's radar cross-section was considerably smaller during this encounter. We measured a total OC cross-section of σ_{OC} = 220 ± 60 km^2, giving a radar albedo estimate of $\hat{\sigma}_{OC} = 0.12 \pm 0.03$ (Table 2). Only a single observation on 7 March 2013 had a radar albedo greater than 0.16. There were hints of bifurcated echoes, suggesting large scale structures, in some of

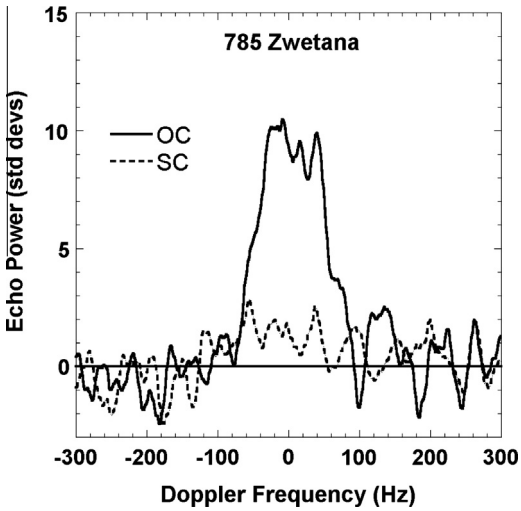

Fig. 17. Sum of CW spectra of 785 Zwetana, smoothed to 20 Hz effective frequency.

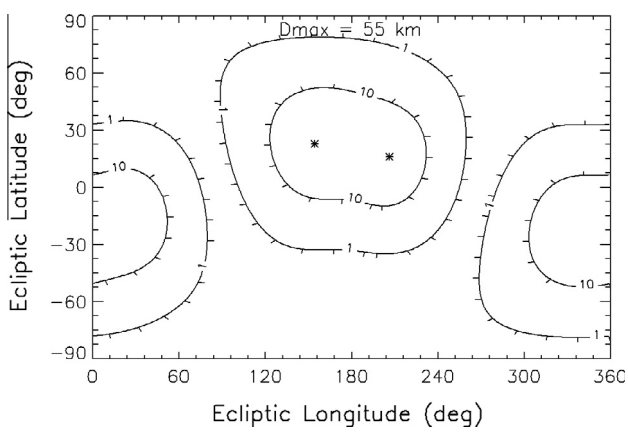

Fig. 18. χ^2 contour plot of pole solutions for Zwetana assuming D_{max} = 55 km, and the radar bandwidths and positions at the time of the radar observations in 2005 and 2013 (shown by a bold asterisk). The true pole is most likely to fall outside the χ^2 = 1 boundaries.

the radar observations and although the SNR was low for these observations, the echo shapes repeated at similar rotation phases. The weighted sum of the 2005 and 2013 observations still has a relatively high radar albedo of $\hat{\sigma}_{OC} = 0.26 \pm 0.07$ and μ_c = 0.17 ± 0.02.

These new observations suggest that Zwetana may not have an intrinsically high radar reflectivity or a metal dominated composition; if it did, we would expect to have seen high radar cross-sections during this encounter as we did in 2005. Instead, the most likely conclusion is that Zwetana has a typical MBA radar reflectivity and an unusual shape or surface structures which, at some aspects, focus or backscatter much more radar energy than expected. Perhaps there are large-scale facets or concavities that were ideally oriented in the 2005 encounter. These regions may also be deficient in regolith so that the reflecting surface is more coherent. Our radar reflectivity model assumes a substantial regolith, but this may not always be a good assumption for smaller MBAs such as Zwetana. Thermal inertia estimates may be able to address this hypothesis.

4. Analysis and discussion

Twenty-nine M-class MBAs have now been observed with radar. In this section, we summarize what we have learned from our observations of these objects. Table 3 and Fig. 19 summarize the basic physical and radar properties of each target.

4.1. Composition, bulk density, and implications for structure

Eleven asteroids, or 38% of our sample, have radar albedos at some or all rotation phases that are consistent with the interpretation that they are dominated by iron–nickel: 16 Psyche (Shepard et al., 2010), 69 Hesperia (Shepard et al., 2011), 92 Undina, 110 Lydia, 129 Antigone (Shepard et al., 2008), 201 Penelope, 216 Kleopatra (Ostro et al., 2000), 347 Pariana (Shepard et al., 2010), 413 Edburga, 758 Mancunia (Shepard et al., 2008), and 779 Nina (Shepard et al., 2010). Based on our most recent results, we have excluded 785 Zwetana from this list (Shepard et al., 2008). The mean radar albedo for these objects is $\hat{\sigma}_{OC} = 0.41 \pm 0.09$, three times higher than the average S-class asteroid (Magri et al., 2007). Eq. (5) suggests a mean surface density of 4.0 g cm^{-3}, consistent with 90–100% NiFe metal and ~50% porosity. Discounting the outliers 83 Beatrix and 572 Rebekka which, in some surveys, have been classified as spectrally primitive D- or C-class (Rebekka) or P-class (Beatrix) asteroids, the mean radar albedo of the remaining objects is 0.22 ± 0.04. For comparison, Magri et al. (2007) find the mean radar albedo for the S- and C-classes to be 0.14 ± 0.04 and 0.13 ± 0.05, respectively. Clearly, even those M-class asteroids that are not dominated by metal still have higher surface bulk densities, and by inference higher metal contents, than the typical MBA. This would be consistent with other possible M-class analogs, most notably enstatite chondrites.

Estimates of the overall bulk density of M-class asteroids are sparse and confusing. 216 Kleopatra, widely believed to be a metal remnant based on its high radar albedo of $\hat{\sigma}_{OC} = 0.6 \pm 0.1$ (Ostro et al., 2000) was recently discovered to have two small moons, allowing for a direct bulk density measurement of 3.6 ± 0.4 g cm^{-3} (Descamps et al., 2011). Eq. (5) suggests the near surface has a bulk

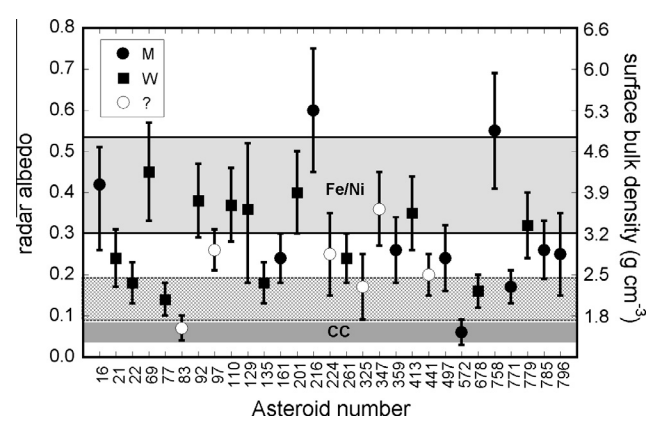

Fig. 19. Radar albedo for every main-belt M-class target observed by radar. Right *y*-axis shows the near-surface bulk density estimated from the Shepard et al. (2010) model. Several regions show range of radar albedos expected for compositional analogs: gray (0.04–0.08) is carbonaceous chondritic (CC); the light gray (0.39–0.55) is the region expected for dominantly metallic asteroids (FE); and the area in-between (0.08–0.39) covers the range of radar albedos expected for enstatite chondritic, stony irons, and high metal carbonaceous chondrites. The hatched region (0.09–0.19) shows where the mean S- and C-class asteroids fall, including one standard deviation (Magri et al., 2007). Solid circles are M-class objects with no observed 3 μm feature. Squares are Rivkin et al. (2000) W-class objects (M-class with a 3 μm feature). Open circles are M-class objects that have not been observed in the 3 μm region. The uncertainties shown are at least ±25%. Asteroids which exhibited significant variation with rotation phase are shown with uncertainties that reflect the range of radar albedos observed and are often asymmetric. To determine whether an asteroid belongs to the Mm-class, we use the highest radar albedo indicated (top of uncertainty bar) except for the case of 785 Zwetana, which is discussed in the text.

density of ~5 g cm^{-3}, considerably higher; however, the two estimates are not necessarily inconsistent because the macro-porosity of the asteroid as a whole is not necessarily equivalent to that of the upper meter or so of the regolith.

Descamps et al. (2008) estimated a similar bulk density of 3.35 ± 0.33 g cm^{-3} for 22 Kalliope, also from the orbital motion of a moon. However, its radar albedo, $\hat{\sigma}_{OC} = 0.18 \pm 0.04$, is not consistent with a metal-dominated composition; Eq. (5) gives a surface bulk density estimate of 2.3 ± 0.3 g cm^{-3}; in this case, the regolith must be considerably more porous than the asteroid as a whole.

More recently, the Rosetta spacecraft flew by 21 Lutetia; the trajectory deflection due to the gravity of Lutetia was used to estimate its mass and provided a bulk density estimate of 3.4 ± 0.3 g cm^{-3} (Patzold et al., 2011). As with Kalliope, Lutetia's radar albedo of $\hat{\sigma}_{OC} = 0.24 \pm 0.06$ is inconsistent with a metal-dominated composition (Magri et al., 2007; Shepard et al., 2008); Eq. (5) gives a surface bulk density estimate of 2.7 ± 0.4 g cm^{-3}. Spectral information suggests Lutetia is more consistent with a chondritic object than metallic (Vernazza et al., 2011), and our radar data are consistent with this interpretation.

The mass of the largest known M-class asteroid, 16 Psyche, has been measured using an integrated ephemeris and orbital perturbations and leads to bulk density estimates of 5–8 g cm^{-3}, but the uncertainties are quite high, ranging from ±3–4 g cm^{-3} (Baer et al., 2011). Ignoring the uncertainties for the moment, these estimates are considerably higher than the other three M-class asteroids and are consistent with the surface density implied by Psyche's high radar albedo, $\hat{\sigma}_{OC} = 0.42 \pm 0.10$ (Shepard et al., 2008).

Ignoring the Psyche results because of the wide uncertainties, we have three relatively robust measurements, statistically indistinguishable, for three very different M-class objects. The Kleopatra density estimate is consistent with a dominantly metal object and bulk porosity of 30–50% (Descamps et al., 2011). The Rosetta observations of Lutetia (Coradini et al., 2011; Vernazza et al., 2011) show the surface of Lutetia to be more like carbonaceous chondrites (CO, CV) or enstatite chondrites – not metal. This has led to the suggestion that Lutetia is at least partially differentiated with an intact core (Weiss et al., 2012), thus explaining the higher overall bulk density and the more modest surface bulk density expected from chondritic regolith. Kalliope, with a diameter of 162 km, is considerably larger than Lutetia and Kleopatra. Its modest radar albedo also suggests a chondritic regolith; is it also a differentiated or partially differentiated object? If so, how did it come by its moon? Is it primordial? Collisions are a possible mechanism, but YORP radiative torques are ineffective on objects this large (Bottke et al., 2006). Additional bulk density estimates of other M-class objects are needed to address these questions.

4.2. The W-class conundrum

Until this study, the only high radar albedo asteroid (Mm) observed to have a 3 μm feature was (129) Antigone (Table 3). However, our new radar observations and additional 3 μm observations by Howell et al. (in preparation) have found six additional W-class asteroids with high radar albedos: (69) Hesperia, (92) Undina, (110) Lydia, (201) Penelope, (413) Edburga, and (779) Nina. One Mm asteroid – Pariana – has no 3 μm observations, so this number could be higher. Counting only those for which we have 3 μm data, we find that nearly two-thirds of the high radar albedo targets (7 of 11) also show evidence of a 3 μm absorption feature.

These observations present a problem. Traditionally, the 3 μm absorption feature has been attributed to hydrated minerals (Jones et al., 1990; Rivkin et al., 1995, 2000). However, the high radar albedo of these objects suggests a high surface bulk density and, by inference, an enormous metal content. This is how a metal core fragment, the canonical interpretation of M-class asteroids, should look to radar. But the high temperatures required for differentiation and the subsequent energy involved in stripping a protoplanet to the core are inconsistent with the presence of hydrated minerals. What alternative explanations are there?

One assumption we have made in this work is that all MBAs have a significant regolith with porosity ~50%. If these particular asteroids had coherent surfaces with little or no regolith, their high radar albedos would be consistent with chondritic compositions and the presence of hydrated minerals would be credible. But based on spacecraft observations and our current understanding of the collisional evolution of main-belt asteroids, we expect a significant regolith on all main-belt asteroids and find this scenario unlikely.

Another scenario sometimes invoked to explain the presence of a 3 μm feature is that these asteroids result from the collision of a metal-rich and more primitive asteroid (Busarev, 1998; Hardersen et al., 2005; Shepard et al., 2008). One argument against this is that high velocity collisions should 'cook' the hydrous minerals, leaving an anhydrous composite. However, lower velocity collisions would not have this difficulty, and there is abundant meteoritical evidence for hydrated xenoliths in otherwise anhydrous meteorites (Gaffey et al., 2002 and references therein). How much material is necessary to exhibit a 3 μm feature? Rivkin et al. (2000) calculate that a few tenths of 1% water content are sufficient.

Telescopic observations by Hasegawa et al. (2003) revealed the unexpected presence of a 3 μm feature on 4 Vesta, an igneous body. And an analysis of Dawn observations of Vesta by Reddy et al. (2012), Prettyman et al. (2012), McCord et al. (2012), and Denevi et al. (2012) found convincing evidence for the surface expression of dark asteroid material and associated hydrated minerals, probably the result of low velocity collisions with one or more primitive hydrated objects. These observations make it credible that some, if not all, of the high-radar albedo W-class objects have similar collisional histories. Can this be tested?

If low-velocity collisions are responsible for adding a 3 μm feature to an M-class asteroid, we would expect to see this in all asteroid types – there is nothing special in this mechanism that would limit it to the M-class. Rivkin et al. (1995) did note a 3 μm feature in several E-class asteroids, another class not expected to have hydrated minerals. But there has been no large scale survey of other anhydrous groups, like the S-class, so this is one way to test this hypothesis.

Vesta showed longitudinal variations in the dark, hydrated material (Reddy et al., 2012). If the implantation is random, another possible test is to look for rotational variations in the 3 μm feature. Although most 3 μm observations are done at single rotational phases, a few have been rotationally resolved, and a small number have been repeated at different viewing aspects. Within those data sets, a few W-class asteroids have been noted to show variations at 3 μm: (21) Lutetia shows a N–S hemispheric difference (Rivkin et al., 2011), and both 22 Kalliope and 55 Pandora show longitudinal variations (Rivkin et al., 2000). Additional rotationally resolved observations at 3 μm are needed.

Could radar be used to test this hypothesis? For collisions between two dominantly silicate asteroids, probably not. Radar is sensitive to the bulk density of the upper few meters of regolith, and silicate regoliths with a wide range of mineralogical compositions will generally look the same. However, if the collision is between a metallic and silicate asteroid, there may be large-scale heterogeneities in regolith bulk density that would be obvious.

Realistically, one only needs a few meters of silicate-dominated mantling over an otherwise metal-rich surface to dramatically reduce the radar albedo, and collections of silicate fines (ponds) observed on both 433 Eros and 25143 Itokawa (Dombard et al.,

2010; Demura et al., 2006) might be a model for this. In these cases, radar would see isolated regions of high and low bulk density as the asteroid rotates. This might manifest as large variations in radar albedo which have been reported for many of our targets (Shepard et al., 2008, 2010, and herein). This heterogeneity might also manifest as radar echoes with more than one peak. As discussed below, we also see this for many of our targets.

4.3. Bifurcated radar echoes, contact binaries, and large-scale density contrasts

We find eleven X/M-class asteroids – 40% of our sample – to display bifurcated radar echoes (Table 3) (We have excluded 22 Kalliope; although binary, it does not display a bifurcated echo). These echo shapes are *sometimes* an indication of a complex shape and potential contact binary system (Ostro et al., 2000), but may also be due to large scale bulk density variations that might occur where there are isolated regions dominated by metals or silicates. We noted earlier that six of the seven Mm/W-class asteroids show bifurcated radar echoes at some rotation phases (Hesperia excepted, but we had only two runs separated by 60° in rotation phase).

Lightcurves with large amplitudes are another possible indicator of a contact binary structure but, by themselves, are insufficient proof of one. Shape modeling from lightcurves is only robust for *convex* shapes at the phase angles obtained for most MBAs (Durech and Kaasalainen, 2003). Of the M-class objects displaying evidence of radar echo bifurcation in our survey, only four have lightcurve amplitudes consistent with contact binaries: Kleopatra ($\Delta m = 1.18$), Antigone (lightcurve $\Delta m = 0.49$), Penelope ($\Delta m = 0.73$), and Edburga ($\Delta m = 0.49$) (Warner et al., 2009a).

Several asteroids in our survey show bifurcated radar echoes, but other observational evidence argues against a contact binary structure. Undina has a strongly bifurcated radar echo, but a low lightcurve amplitude ($\Delta m = 0.17$) over a wide range of apparitions. 779 Nina also shows strongly bifurcated structure in its radar echoes, but it looks equant in radar delay-Doppler imaging and its lightcurve amplitude, like Undina, is also modest ($\Delta m = 0.25$). Similarly, we see strongly bifurcated radar echoes from 110 Lydia, but failed to see either a contact binary or even elongate object with adaptive optics imaging; its lightcurve amplitude is also quite modest ($\Delta m = 0.20$). The best explanation for these observations is that they are asteroids with large-scale variations in regolith properties – metal-rich versus silicate-rich – as described in the previous section. It may require a concerted campaign of lightcurve, radar, and rotationally resolved spectral observations along with AO imaging to test this hypothesis further.

5. Future opportunities

A number of newer complementary techniques are increasingly directed toward the study of the M-class including thermal emission spectroscopy (Emery and Lim, 2011; Crane et al., 2012), thermal interferometry (Matter et al., 2013), and adaptive optics (Drummond and Christou, 2008; Descamps et al., 2011). There is also at least one proposal for a spacecraft mission to the M-class Asteroid 16 Psyche (Elkins-Tanton et al., 2014).

Within the next few years, there are only a few X- or M-class asteroids visible from Arecibo that we have not yet observed. In late 2014, there are opportunities to observe 475 Ocllo (X), 757 Portlandia (X), 55 Pandora (M/W), and 1407 Lindelof (X). In 2015, there are opportunities to observe 75 Eurydike (M), and re-observe 69 Hesperia (M/W), 224 Oceana (M), 441 Bathilde (M), 77 Frigga (M/W), 678 Fredegundis (M/W), and 16 Psyche (M). The Psyche observations should have SNRs sufficient for coarse radar imaging.

Acknowledgments

MKS and BEC acknowledge support from NSF AST-0908098. AWH and BDW acknowledge support from NASA NNG-10AL352G/NNX13AP56G and NSF AST-1032896/AST-1210099. We thank V. Reddy and J. Emery for their reviews. We also thank the following for generously contributing some of their Keck AO time to observe Lydia: F. Morales, I. de Pater, H. Hammel, and K. de Kleer with assistance from C. Neyman, P. Tamblyn, B. Carry, and B. Enke. Arecibo Observatory is operated by SRI International under a cooperative agreement with NSF and in alliance with Ana G. Mendez-Univ. Metropolitana and USRA. The Arecibo Planetary Radar Program is supported by the National Aeronautics and Space Administration under Grant No. NNX12AF24G issued through the Near Earth Object Observations Program. We thank the Arecibo operators and staff for their help in observing. Some of this work was performed at the Jet Propulsion Laboratory, California Institute of Technology, under contract with the National Aeronautics and Space Administration. This material is based in part upon work supported by the National Aeronautics and Space Administration (NASA) under the Science Mission Directorate Research and Analysis Programs.

References

Baer, J., Chesley, S.R., Matson, R.D., 2011. Astrometric masses of 26 asteroids and observations on asteroid porosity. Astron. J. 141. Article ID: 143, 12 pp.
Bell, J.F., Davis, D.R., Hartmann, W.K., Gaffey, M.J., 1989. Asteroids: The big picture. In: Binzel, R.P., Gehrels, T., Matthews, M.S. (Eds.), Asteroids II. Univ. of Arizona, Tucson, pp. 921–948.
Belskaya, I.N., Lagerkvist, C.I., 1996. Physical properties of M class asteroids. Planet. Space Sci. 44, 783–794.
Benner, L.A.M., Ostro, S.J., Magri, C., Nolan, M.C., Howell, E.S., Giorgini, J.D., Jurgens, R.F., Margot, J.L., Taylor, P.A., Busch, M.W., Shepard, M.K., 2008. Near-Earth asteroid surface roughness depends on compositional class. Icarus 198, 294–304.
Birlan, M., Vernazza, P., Nedelcu, D.A., 2007. Spectral properties of nine M-type asteroids. Astron. Astrophys. 475, 747–754.
Bottke Jr., W.F., Vokrouhlicky, D., Rubincam, D.P., Nesvorny, D., 2006. The Yarkovsky and YORP effects: Implications for asteroid dynamics. Annu. Rev. Earth Planet. Sci. 34, 157–191.
Bus, S.J., Binzel, R.P., 2002. Phase II of the small main-belt asteroid spectroscopic survey: A feature-based taxonomy. Icarus 158, 146–177.
Busarev, V.V., 1998. Spectral features of M-asteroids: 75 Eurydike and 201 Penelope. Icarus 131, 32–40.
Chapman, C.R., Salisbury, J.W., 1973. Comparisons of meteorite and asteroid spectral reflectivities. Icarus 19, 507–522.
Clark, B.E., Bus, S.J., Rivkin, A.S., Shepard, M.K., Shah, S., 2004. Spectroscopy of X-type asteroids. Astron. J. 128, 3070–3081.
Cloutis, E.A., Gaffey, M.J., Smith, D.G.W., Lambert, R.St.J., 1990. Metal silicate mixtures: Spectral properties and applications to asteroid taxonomy. J. Geophys. Res. 95, 8323–8338.
Coradini, A. et al., 2011. The surface composition and temperature of Asteroid 21 Lutetia as observed by Rosetta/VIRTIS. Science 334, 492–494.
Crane, K.T., Emery, J.P., Lim, L.F., 2012. Shape and thermal modeling of a selection of M-type asteroids. Lunar Planet. Sci. 43. Abstract #1425.
DeMeo, F.E., Binzel, R.P., Slivan, S.M., Bus, S.J., 2009. An extension of the Bus asteroid taxonomy into the near-infrared. Icarus 202, 160–180.
Demura, H. et al., 2006. Pole and global shape of 2513 Itokawa. Science 312, 1347–1349.
Denevi, B.W. et al., 2012. Pitted terrain on Vesta and implications for the presence of volatiles. Science 338, 246–249.
Descamps, P. et al., 2008. New determination of the size and bulk density of the binary Asteroid 22 Kalliope from observations of mutual eclipses. Icarus 196, 578–600.
Descamps, P. et al., 2011. Triplicity and physical characteristics of Asteroid (216) Kleopatra. Icarus 211, 1022–1033.
Dombard, A.J., Barnouin, O.S., Prockter, L.M., Thomas, P.C., 2010. Boulders and ponds on the Asteroid 433 Eros. Icarus 210, 713–721.
Drummond, J., Christou, J., 2008. Triaxial ellipsoid dimensions and rotational poles of seven asteroids from Lick Observatory adaptive optics images, and of Ceres. Icarus 197, 480–496.
Dunham, D.W., Herald, D., Frappa, E., Hayamizu, T., Talbot, J., Timerson, B., 2014. Asteroid Occultations V12.0 EAR-A-3-RDR-OCCULTATIONS-V12.0. NASA Planetary Data System.
Durech, J., Kaasalainen, M., 2003. Photometric signatures of highly nonconvex and binary asteroids. Astron. Astrophys. 404, 709–714.

Durech, J. et al., 2007. Physical models of ten asteroids from an observers' collaboration network. Astron. Astrophys. 465, 331–337.
Durech, J., Sidorin, V., Kaasalainen, M., 2010. DAMIT: A database of asteroid models. Astron. Astrophys. 513 (A46), 13. http://dx.doi.org/10.1051/0004-6361/200912693.
Elkins-Tanton et al., 2014. Journey to a metal world: Concept for a Discovery mission to Psyche. Lunar Planet. Sci. 45. Abstract #1253.
Emery, J.P., Lim, L.F., 2011. Thermal emission spectroscopy of M-type asteroids: How many are metallic? EPSC-DPS Joint Meeting, Nantes, France, p. 1438.
Fornasier, S., Clark, B.E., Dotto, E., 2011. Spectroscopic survey of X-type asteroids. Icarus 214, 131–146.
Gaffey, M.J., 1976. Spectral reflectance characteristics of the meteorite classes. J. Geophys. Res. 81, 905–920.
Gaffey, M.J., McCord, T.B., 1979. Mineralogical and petrological characterizations of asteroid surface materials. In: Gehrels, T. (Ed.), Asteroids. Univ. of Arizona Press, Tucson, pp. 688–723.
Gaffey, M.J., Cloutis, E.A., Kelley, M.S., Reed, K.L., 2002. Mineralogy of asteroids. In: Bottke, W.F., Jr., Cellino, A., Paolicchi, P., Binzel, R.P. (Eds.), Asteroids III. University of Arizona, Tucson, pp. 183–204.
Garvin, J.B., Head, J.W., Pettengill, G.H., Zisk, S.H., 1985. Venus global radar reflectivity and correlations with elevation. J. Geophys. Res. 90, 6859–6871.
Hanus, J. et al., 2011. A study of asteroid pole-latitude distribution based on an extended set of shape models derived by the lightcurve inversion method. Astron. Astrophys. 530, A134 16 pp.
Hanus, J., Marchis, F., Durech, J., 2013. Sizes of main-belt asteroids by combining shape models and Keck adaptive optics observations. Icarus 226, 1045–1057.
Hardersen, P.S., Gaffey, M.J., Abell, P.A., 2005. Near-IR spectral evidence for the presence of iron-poor orthopyroxenes on the surfaces of six M-type asteroids. Icarus 175, 141–158.
Hardersen, P.S., Cloutis, E.A., Reddy, V., Mothe-Diniz, T., Emery, J.P., 2011. The M-/X-asteroid menagerie: Results of an NIR spectral survey of 45 main-belt asteroids. Meteorit. Planet. Sci. 46, 1910–1938.
Hasegawa, S. et al., 2003. Evidence of hydrated and/or hydroxylated minerals on the surface of Asteroid 4 Vesta. Geophys. Res. Lett. 30 (21), PLA 21–2–4.
Jones, T.D., Lebofsky, L.A., Lewis, J.S., Marley, M.S., 1990. The composition and origin of the C, P, and D asteroids: Water as a tracer of thermal evolution in the outer belt. Icarus 88, 172–192.
Lebofsky, L., 1989. Wavelength dependence of IRAS asteroid diameters and albedos. Icarus 78, 355–362.
Lupishko, D.F., Belskaya, I.N., 1989. On the surface composition of the M-type asteroids. Icarus 78, 395–401.
Magri, C., Consolmagno, G.J., Ostro, S.J., Benner, L.A.M., Beeney, B.R., 2001. Radar constraints on asteroid regolith properties using 433 Eros as ground truth. Meteorit. Planet. Sci. 36, 1697–1709.
Magri, C., Nolan, M.C., Ostro, S.J., Giorgini, J.D., 2007. A radar survey of main-belt asteroids: Arecibo observations of 55 object during 1999–2003. Icarus 186, 126–151.
Masiero, J.R. et al., 2011. Main belt asteroids with WISE/NEOWISE. I. Preliminary albedos and diameters. Astrophys. J. 741. Article ID: 68, 20 pp.
Matter, A., Delbo, M., Carry, B., Ligori, S., 2013. Evidence of a metal-rich surface for the Asteroid (16) Psyche from interferometric observations in the thermal infrared. Icarus 226, 419–427.
McCord, T.B. et al., 2012. Dark material on Vesta from the infall of carbonaceous volatile-rich material. Nature 491, 83–86.
Ockert-Bell, M.E., Clark, B.E., Shepard, M.K., Rivkin, A., Binzel, R., Thomas, C.A., DeMeo, F.E., Bus, S.J., Shah, S., 2008. Observations of X/M asteroids across multiple wavelengths. Icarus 195, 206–219.
Ockert-Bell, M.E., Clark, B.E., Shepard, M.K., Isaacs, R.A., Cloutis, E., Fornasier, S., Bus, S.J., 2010. The composition of M-type asteroids: Synthesis of spectroscopic and radar observations. Icarus 210, 674–692.
Ostro, S.J., Campbell, D.B., Shapiro, I.I., 1985. Mainbelt asteroids: Dual polarization radar observations. Science 229, 442–446.
Ostro, S.J. et al., 2000. Radar observations of Asteroid 216 Kleopatra. Science 288, 836–839.
Ostro, S.J. et al., 2005. Radar observations of Itokawa in 2004 and improved shape estimation. Meteorit. Planet. Sci. 40, 1563–1574.
Patzold, M. et al., 2011. Asteroid 21 Lutetia: Low mass, high density. Science 334, 491. http://dx.doi.org/10.1126/science.1209389.
Pravec, P., Harris, A.W., 2007. Binary asteroid population. 1. Angular momentum content. Icarus 190, 250–259.
Prettyman, T.H. et al., 2012. Elemental mapping by Dawn reveals exogenic H in Vesta's regolith. Science 338, 242–246.
Reddy, V. et al., 2012. Delivery of dark material to Vesta via carbonaceous chondritic impacts. Icarus 221, 544–559.
Rivkin, A.S., Howell, E.S., Britt, D.T., Lebofsky, L.A., Nolan, M.C., Branston, D.D., 1995. 3-μm spectrophotometric survey of M and E-class asteroids. Icarus 117, 90–100.
Rivkin, A.S., Howell, E.S., Lebofsky, L.A., Clark, B.E., Britt, D.T., 2000. The nature of M-class asteroids from 3-μm observations. Icarus 145, 351–368.
Rivkin, A.S., Clark, B.E., Ockert-Bell, M., Volquardsen, E., Howell, E.S., Bus, S.J., Thomas, C.A., Shepard, M.K., 2011. Asteroid 21 Lutetia at 3 μm: Observations with IRTF SpeX. Icarus 216, 62–68.
Shepard, M.K. et al., 2008. A radar survey of M- and X-class asteroids. Icarus 195, 184–205.
Shepard, M.K., Clark, B.E., Ockert-Bell, M., Nolan, M.C., Howell, E.S., Magri, C., Giorgini, J.D., Benner, L.A.M., Ostro, S.J., Harris, A.W., Warner, B.D., Stephens, R.D., Mueller, M., 2010. A radar survey of M- and X-class asteroids II. Summary and synthesis. Icarus 208, 221–237.
Shepard, M.K., Harris, A.W., Taylor, P.A., Clark, B.E., Ockert-Bell, M., Nolan, M.C., Howell, E.S., Magri, C., Giorgini, J.D., Benner, L.A.M., 2011. Radar observations of Asteroids 64 Angelina and 69 Hesperia. Icarus 215, 547–551.
Stephens, R.D., Warner, B.D., Shepard, M.K., Harris, A.W., 2008. Lightcurve and radar observations and analysis of 11 Parthenope and 678 Fredegundis. Bull. Am. Astron. Soc. (abstract) #28.16.
Takir, D., Hardersen, P.S., Gaffey, M.J., 2008. The near-infrared spectroscopy of two M-class main belt asteroids, 77 Frigga and 325 Heidelberga. Lunar Planet. Sci. 39. Abstract #1084.
Tedesco, E.F., Noah, P.V., Noah, M., 2002. The supplemental IRAS minor planet survey. Astron. J. 123, 1056–1085.
Tholen, D., 1984. Asteroid Taxonomy from Cluster Analysis of Photometry. PhD Thesis, Univ. of Arizona, Tucson. 150pp.
Torppa, J., Kaasalainen, M., Michalowski, T., Kwiatkowski, T., Kryszczynska, A., Denchev, P., Kowalski, R., 2003. Shapes and rotational properties of thirty asteroids from photometric data. Icarus 164, 346–383.
Usui, F. et al., 2011. Asteroid catalog using Akari: AKARI/IRC mid-infrared asteroid survey. Publ. Astron. Soc. Jpn. 63, 1117–1138.
Vernazza, P., Lamy, P., Groussin, O., Hiroi, T., Jorda, L., King, P.L., Izaw, M.R.M., Marchis, F., Birlan, M., Brunetto, R., 2011. Asteroid (21) Lutetia as a remnant of Earth's precursor planetesimals. Icarus 216, 650–659.
Vilas, F., 1994. A cheaper, faster, better way to detect water of hydration on Solar System bodies. Icarus 111, 456–467.
Warner, B.D., Harris, A.W., Pravec, P., 2009a. The asteroid lightcurve database. Icarus 202, 134–146, See also http://www.minorplanetcenter.net/iau/lists/LightcurveDat.html for up-to-date values and references to individual lightcurves.
Warner, B.D., Stephens, R.D., Harris, A.W., Shepard, M.K., 2009b. Coordinated lightcurve and radar observations of 110 Lydia and 135 Hertha. Minor Planet Bull. 36, 38–39.
Weiss, B.P. et al., 2012. Possible evidence for partial differentiation of asteroid Lutetia from Rosetta. Planet. Space Sci. 66, 137–146.